

Rheological stratification in experimental free-surface flows of granular-liquid mixtures

Aronne Armanini¹, Hervé Capart², Luigi Fraccarollo¹, and Michele Larcher¹

¹ Dipartimento di Ingegneria Civile e Ambientale and Centro Universitario per la Difesa Idrogeologica dell'Ambiente Montano (CUDAM), Università degli Studi di Trento, Italy.

² Department of Civil Engineering and Hydrotech Research Institute, National Taiwan University, Taiwan. Former affiliation: Department of Civil and Environmental Engineering, Université catholique de Louvain, and Fonds National de la Recherche Scientifique, Belgium.

Abstract

Laboratory experiments are conducted to study the rheological behaviour of high-concentration granular-liquid mixtures. Steady uniform free-surface flows are obtained using a recirculating flume. Cases in which a loose deposit forms underneath the flow are contrasted with runs for which basal shear occurs along the flume bottom. The granular motions are observed through the channel sidewall, and analysed with recently developed Voronoï imaging methods. Depth profiles of mean velocity, solid concentration, and granular temperature are obtained, and complemented by stress estimates based on force balance considerations. These measurements are used to probe variations in rheological behaviour over depth, and to clarify the role of the granular temperature. The flows are found to evolve a stratified structure. Distinct sub-layers are characterised by either frictional or collisional behaviour, and transitions between one and the other occur at values of the Stokes number which suggest that viscous effects intervene. The observed frictional behaviour is consistent with shear cell tests conducted at very low shear rates. On the other hand, the collisional data corroborate both the Bagnold description and the more recent kinetic theories of granular flows, provided that one accounts for the inertia of the interstitial liquid.

1. Introduction

Gravity-driven flows of high-concentration granular-liquid mixtures intervene in a wide variety of geomorphological and industrial processes. Within the scope of civil engineering, natural flow examples include sediment-laden currents, debris surges and soil flowslides, while technological applications include the handling of dredging slurries and fresh concrete. A key feature of these flows is the highly inhomogeneous rheological behaviour of the granular-liquid mixture.

A typical situation, examined in depth in the present paper, is illustrated on Fig. 1. Here a moving layer of grains and liquid flows over a static layer of loose material. The two layers are composed of identical solid and liquid constituents, yet respond differently to shearing action due to contrasts in solid concentration and normal stress conditions. In other situations, granular-liquid mixtures may undergo repeated transitions between states of flow and no-flow. For instance, a debris flow slurry may freeze into place before being remobilized by further debris surges. Such rheological transitions play a key role in many earth surface processes.

The present work seeks to address this issue by carrying out detailed measurements of simplified laboratory experiments. The experiments involve steady uniform free-surface flows of pellet-water mixtures in a recirculating flume apparatus. As in the pioneering experiments of Bagnold (1954), attention is restricted to simply sheared dispersions of identical solid grains in a Newtonian liquid. Whereas Bagnold conducted his experiments with neutrally buoyant solid grains, however, our experiments involve pellets which are denser than water. While Bagnold sought to avoid gravity effects, our aim is precisely to examine the inhomogeneous structure induced when dense grains are dispersed in a lighter liquid.

The restriction to identical particles in a Newtonian liquid represents a strong idealisation.

Field cases commonly involve heterogeneous particles in a non-Newtonian fluid. Naturally occurring debris flows, for instance, are often composed of poorly sorted clasts embedded in a mud matrix. Likewise, flows of practical interest may involve modes of deformation which are more complicated than simple shear. In particular, volumetric deformations of the granular phase may play an important role due to their effect on the liquid pore-pressure (Iverson, 1997). Despite their practical significance, these aspects will not be addressed here.

Granular-liquid flows remain challenging even without such complications. Responding to applied stresses, a granular phase composed of identical particles may behave alternatively like a solid, a liquid or a gas (Jaeger *et al.* 1996; Goldhirsch 2003). The coupled motions of the interstitial liquid may further strongly affect the properties of the deforming mixture (Koch & Hill 2001). Despite the simplified character of the present experiments, their interpretation will thus raise a number of fundamental questions. How do discrete grains interact with each other and with the continuous embedding fluid? How do these interactions lead to distinct rheological behaviours? How do these distinct behaviours co-exist within inhomogeneous flows?

In recent years, such questions have been addressed in some depth for two related physical systems: dry granular flows, and bubbly flows. These share many of the features of granular-liquid flows, but take the density ratio of the disperse and continuous phases to distinct limits: $\rho_d / \rho_c \gg 1$ for dry granular flows, and $\rho_d / \rho_c \ll 1$ for bubbly flows. In these cases, simplifications arise because either the inertia or the vorticity of the continuous phase can be neglected (Koch & Hill 2001). For both these systems, theoretical approaches based on the kinetic theory of dense gases (Chapman & Cowling 1971) have been successfully applied to rapid flows dominated by collisional interactions. For dry granular flows, milestones include the works of Ogawa (1978), Savage and Jeffrey (1981) and Jenkins

and Savage (1983). More recently, the effects of an interstitial gas phase have also been addressed (e.g. Sangani *et al.* 1996). For bubbly flows, on the other hand, recent developments include the studies of Russo and Smereka (1996), and Kang *et al.* (1997).

For both dry granular flows and bubbly flows, theoretical results have been corroborated and extended by dynamical simulations (Campbell & Brennen 1985; Walton & Braun 1986; Smereka 1993; Sangani & Didwania 1993). Computational experiments have further highlighted possible transitions in behaviour and the development of structure in inhomogeneous flows (Zhang & Campbell 1992; Savage & Dai 1993; Smereka 1993; Sangani & Didwania 1993; Zhang & Rauenzahn 1997; Aharonov & Sparks 1999). A number of laboratory studies have also provided additional information regarding dry granular flows. Most measurements of individual particle motions have been obtained for two-dimensional analogues such as monolayers of particles held between parallel plates (Drake 1991; Elliott *et al.* 1998; Azanza *et al.* 1999). Yet detailed experimental results have also been gathered for 3D flows. These include measurements of the local particle motions in the vicinity of a sidewall (Ahn *et al.* 1991; Natarajan *et al.* 1995; Hsiau & Jang 1998), and observations of global flow behaviour in wide channels (Louge & Keast 2001; Ancey 2002).

Studies of collisional flows owe much to the pioneering work of Bagnold (1954), who showed that stresses in rapidly sheared granular dispersions exhibit a quadratic dependence on the deformation rate. As mentioned earlier, the work of Bagnold (1954) was based on experiments with neutrally buoyant particles in water, for which the ratio ρ_d / ρ_c was precisely unity. Paradoxically, ensuing efforts have been less successful at addressing liquid-granular flows ($\rho_d / \rho_c \sim 1$) than at treating dry grains and bubbles. Despite Bagnold's early breakthrough, it has proven difficult to probe granular-liquid mixtures at a level of detail comparable to the dry granular and bubbly flow studies cited above. Direct computations of

granular-liquid flows, for instance, remain very difficult to conduct. Impressive recent efforts include the fluidization studies of Kalthoff *et al.* (1997), and Pan *et al.* (2002), based on coupling the granular dynamics together with the Navier-Stokes equations for the interstitial fluid in the evolving domain. For shear flows, such detailed computations have not yet appeared. Discrete particle simulations have been conducted, but rely on simplified models of inter-particle and particle-fluid interactions (Yeganeh *et al.* 2000; Drake & Calantoni 2001).

The present investigation therefore turns to laboratory experiments. Past empirical studies of granular-liquid flows include those of Savage and McKeown (1983), Hanes and Inman (1985), Davies (1988), Tubino and Lanzoni (1993), Aragon (1995), Asano (1995), Sumer *et al.* (1996), Bakhtiary and Asano (1998), and Courrech du Pont *et al.* (2003). In order to probe the inhomogeneous structure of liquid-granular flows, the present work differs from past studies in two respects: the choice of flow configuration and the level of detail sought. Previous experimental studies have examined solid-liquid flows in annular shear cells (Bagnold 1954; Savage & McKeown 1983), closed ducts (Sumer *et al.* 1996; Bakhtiary & Asano 1998), non-recirculatory chutes (Aragon 1995), or rotating drums (Courrech du Pont *et al.* 2003). Here a novel recirculatory flume introduced by Armanini *et al.* (2000) is used to obtain rectilinear open-channel flows in steady uniform conditions. The special flume permits flows with and without loose deposit at the base. Most importantly, the parallel flow conditions allow local stresses within the bulk mixture to be estimated based on simple force balance considerations.

Recently developed digital imaging methods are then used to obtain a detailed characterisation of the local flow kinematics, as seen through the flume side wall. In contrast with previous attempts at applying particle-tracking techniques to dense granular flows (Natarajan *et al.* 1995; Hsiau & Jang 1998; Azanza *et al.* 1999), the methods are able to

automatically resolve individual grain motions without being limited to sparse tracer particles or two-dimensional dispersions. This is achieved through the use of a robust pattern-matching algorithm based on the Voronoï diagram (Okabe *et al.* 1992; Capart *et al.* 2002). In addition to mean velocity and solid concentration profiles, the methods yield detailed granular temperature data (a measure of the strength of velocity fluctuations) averaged from samples of up to 10^5 individual measurements per run.

Thanks to the flow configuration and imaging methods used, a comprehensive characterisation of the flow structure can be derived for different regimes. The data set documented in the present paper includes 16 different runs. For each of these runs, the measurements obtained include detailed depth profiles of mean velocity, solid concentration, and velocity fluctuations, complemented by estimates of shear and normal stresses. These data will be interpreted in light of available theories and compared with corresponding information regarding dry and bubbly flows. The ultimate aim of the data analysis will be to construct a global interpretation of the rheological structure of the observed flows.

The paper is organised as follows. Section 2 documents in detail the apparatus, materials and methods used for the experiments, as well the range of conditions covered by the tests. Section 3 is then devoted to the presentation of the measurements and section 4 to their rheological interpretation. The concluding section, finally, aims to provide an overall synthesis.

2. Experimental conditions and methods

2.1. Laboratory flume and granular material properties

Figure 2 shows the special laboratory flume developed at the Hydraulics Laboratory of the Università degli Studi di Trento (Armanini *et al.* 2000) for the study of steady uniform

granular-liquid flows. The apparatus is composed of two main components: the first is a glass-walled open channel, in which downslope flows are observed; the second is an external conveyor belt, connected to the channel by chute guides, which recirculates upslope both water and sediment. The channel can be tilted at angles going from 0° to 25°. It has a length of 6 m and a width of 40 cm, narrowed down to 20 cm for the present study by placement of a glass partition. The channel floor is artificially roughened by glued coarse sand. Imaging measurements are made 2 m upstream of the channel outlet, by filming the flow through the sidewalls and from the top. To view the basal flow condition at the centre of the cross-section, a small port-hole is pierced through the opaque channel floor. The external conveyor system has a length of 8.40 m, and is equipped with a 50 cm wide V-shaped flexible belt that can be operated at speeds of up to 5 m/s. The belt is aligned with the flume and tilted slightly more, in order for the material to be conveniently collected and refed. A hopper is placed at the flume outlet to collect water and grains. The system permits steady flows at discharges of up to 20 l/s, without limitations on the solids content.

During an experimental run, the set-up forms a closed loop in which a determined volume of water and granular material circulates. Provided it is sufficiently high, the speed of the conveyor belt does not noticeably influence the flow inside the channel. For the present experiments, fast belt speeds of 5 m/s and 2.5 m/s were adopted for test runs 5-11 and 38-106, respectively (see Table 2). The throughput is then controlled solely by the volumes of water and sediment inside the system. When these parameters are kept constant (and aside from certain regimes which exhibit a pulsating behaviour, see infra), the recirculating flow settles to a steady state within a matter of minutes. Camera and lighting adjustments can then be made, and video footage acquired. At the end of a run, the channel outflow is diverted to a trap during a short timed interval (of 5 to 10 s) in order to independently measure the water and granular discharges.

Cylinder-shaped extruded PVC pellets were selected as granular material for the present tests. The particles have an equivalent spherical diameter $d = 3.7$ mm and a specific gravity $s = \rho_s / \rho_w = 1.54$. The material is lighter than natural sediment materials ($s \approx 2.65$), hence more readily entrained by water, facilitating observation. The white colour of the PVC pellets contrasts well with darker surrounding fluid, and is ideal for the automated imaging measurements presented in the next section. For quick characterisation of the flow deformation, the white particles were seeded with a small proportion of black particles (1%). These black particles facilitate eye observation, and can be manually tracked on video images to get a preliminary idea of the mean velocity profile across the depth. The sparse black grains are ignored by the automated algorithms, which instead capture the motions of the dense dispersion of white grains.

Various characterisation tests were performed to determine the properties of the individual particles and their bulk assembly. These tests and their results are summarised in Table 1 and Figures 3-4. Properties of special interest for the ensuing analysis include permeability, capillary rise, and critical angle of friction. Note that due to their relatively large size and greater elasticity, the PVC pellets differ significantly from the natural sediment grains handled in standard geotechnical tests, and the corresponding procedures had to be adapted. For instance, typical methods of sample preparation involving controlled material compaction with a hammer could not be applied because of elastic rebound.

The simple shear tests illustrate both the usefulness of geotechnical characterisation and the need for caution. These tests were performed on our behalf by Dr. J.-F. Vanden Berghe, using a direct simple shear apparatus developed by the Norwegian Geotechnical Institute. The

apparatus allows the shearing of a soil under conditions of constant volume and uniform shear strain throughout the sample. The specimen is confined within a wire reinforced rubber membrane which prevents radial deformation. Horizontal deformation is forced by translating the base relative to the fixed specimen top at the very slow speed of 0.03 mm/min, and an actuator continuously adjusts the normal force to prevent vertical deformation. The material is saturated with water, maintained at atmospheric pressure throughout the test. Shear and effective normal stresses are measured during the deformation. Details of the procedure and typical results for natural materials are documented in Dyvik *et al.* (1987), and Vanden Berghe *et al.* (2001).

Stress path results for the PVC material at different void ratios $e = (1 - c_s)/c_s$ are plotted on Fig. 3. For dense sand of a given void ratio, stress paths typically converge onto a proportional path (a straight line passing through the origin) rising up to the so-called steady state point where stresses remain constant under continuing deformation (Castro & Poulos 1977). Tests for different void ratios yield separate steady state points which fall onto a unique straight line, and the inclination of this line defines the critical angle of friction (see e.g. Bauer 1996). For the PVC material, curved stress paths are obtained rather than straight lines. Nonetheless, the void ratio-dependent steady state points (reached after a shear strain of the order of 50 %) do approximately collapse onto a straight line, from which a critical friction angle $\theta_c \approx 31^\circ$ can be deduced. This result is very useful because steady simple shear approximates closely the local deformation conditions in the flume experiments. This will allow comparison of the steady state stress ratios of the very slow direct shear tests with those of the channel flows. Some degree of caution will however be necessary when invoking the shear cell tests to interpret the flume experiments. Due to the small sample size, the smallest stresses that could be applied and resolved in the simple shear apparatus are roughly 100 times larger than those experienced by the material during the free-surface flow.

2.2. Voronoï imaging measurements

Flows are imaged through the transparent flume sidewall using a Redlake high-speed camera. At the chosen video rate of 250 frames per second, the digital images have a resolution of 420 × 480 pixels × 256 levels of grey. To prevent motion-induced blur, the camera shutter is set at 1/2500 s. For runs with a very thick moving layer, the top and bottom halves of the flow (with 20 % overlap) are filmed separately one after the other in quick succession. Finally a mirror can be placed above the channel to acquire top view images of the flow free surface. The image analysis is performed entirely off-line.

The motions and arrangements of visible particles are captured using the imaging methods of Capart *et al.* (2002), developed specifically for granular flows. The digital frames are first convoluted with a Laplacian-of-Gaussian filter (Jähne 1995). To highlight particle images, the filter width is set equal to the pixel diameter of the grains. Particles positions are then obtained by pinpointing local brightness maxima to subpixel accuracy. Tracking of the particles on successive frames is performed using a pattern-based matching principle based on the Voronoï tessellation (Okabe *et al.* 1992; Capart *et al.* 2002). The method is illustrated on Fig. 5: Voronoï diagrams are constructed on the sets of particle positions identified on separate frames; particles on one frame and the next are then paired based on the shape similarity of their Voronoï cells; velocities are finally derived from the corresponding displacements using the straightforward approximation

$$\mathbf{v}_i^{(n)} = \frac{\mathbf{r}_i^{(n+1)} - \mathbf{r}_i^{(n)}}{\Delta t}, \quad (1)$$

where $\mathbf{r}_i^{(n)} = (x_i^{(n)}, y_i^{(n)})$ is the 2D position of the i -th particle at time $t^{(n)}$, $\mathbf{v}_i^{(n)} = (u_i^{(n)}, v_i^{(n)})$ is the corresponding in-plane velocity, and the x and y axes are oriented in directions parallel and perpendicular to the mean flow direction, respectively (the 2D images of the near-wall

flow do not allow measurement of the out-of-plane velocity component $w_i^{(n)}$).

Transformation from pixel to physical coordinates is easily performed based on a calibrated scale factor and a rotation adjustment.

Estimate (1) is subject to three sources of error which may significantly affect the velocity fluctuation statistics: (i) pair mismatches arising from incorrect tracking can generate spurious outliers; (ii) the limited accuracy of particle positioning induces some artificial noise; (iii) the finite time resolution Δt damps high-frequency physical fluctuations. To deal with the first source of error, post-processing steps are used to eliminate mismatch outliers on the basis of trajectory and neighbourhood regularity (see Capart *et al.* 2002). To avoid statistical bias due to excessive pruning, the rejection criteria are set to be no stricter than twice the interquartile interval of the corresponding velocity distribution, and affect less than 5 % of the data. Errors of type (ii) and (iii), by contrast, cannot be eliminated directly. Their effect on the flow statistics, however, can be estimated and compensated for by exploiting the Lagrangian velocity auto-correlation signals. The procedures developed for this purpose are presented in the appendix.

Sample velocity measurements obtained with the above techniques are shown on Fig. 6. The results illustrate the various features which make particle tracking difficult in rapid granular flows. First, large interframe displacements (shown true to scale) relative to interparticle distances are observed in the upper part of the flow (Fig. 6b). In such conditions, the simplest tracking algorithms based on minimum displacement (e.g. Guler *et al.* 1999) break down. The rather irregular motions documented on Fig. 6c,d also thwart more sophisticated PTV methods involving trajectory-based matching (e.g. Sethi & Jain 1987). Intense shear (up to $\sim 40 \text{ s}^{-1}$ in this example) is further observed through most of the flow layer, a condition

known to pose problems to conventional PIV methods (Huang *et al.* 1993). An attempt to apply PIV to the present flows failed for shear rates higher than 25 s^{-1} . The Voronoï methods, by contrast, perform well throughout. Vector yields are excellent. On average for the run shown, 367 particles per frame are identified, 92 % of which are successfully tracked to the next frame.

The 2D images are also used to estimate the 3D volumetric granular concentration c_s near the wall. As explained in Capart *et al.* (2002), the point density of visible particles per unit image surface is a poor indicator of 3D concentration, due to the prevalence of occlusion effects. Instead, characteristics of the local particle arrangement can be exploited using the Voronoï diagram built on the particle centres. As the solid concentration rises, excluded volume effects tend to organise a dispersion of identical particles into an increasingly ordered assembly. A measure of this ordering is furnished by the roundness of the Voronoï polygons (see Fig. 5b), defined as the ratio $\xi = 4\pi A / P^2$ where A is the polygon area and P its perimeter. On average, the solid concentration was found by Capart *et al.* (2002) to vary with roundness according to the following normalised power-law relation:

$$\frac{c_s}{c_s^{(\text{rcp})}} = \left(\frac{\xi - \xi^{(\text{min})}}{\xi^{(\text{rcp})} - \xi^{(\text{min})}} \right)^b \quad (2)$$

where c_s = solid concentration, i.e. the volumetric fraction of solid material in the mixture; superscripts (rcp) and (min) designate the state of random close packing and the dilute state, respectively. As $c_s \rightarrow 0$, particle positions become uncorrelated and the corresponding roundness value $\xi^{(\text{min})} = 0.73$ can be evaluated by Monte-Carlo simulations of a Poisson point process (see Okabe *et al.* 1992). The other parameters were calibrated by Capart *et al.* (2002) on the basis of fluidisation cell tests, yielding values $\xi^{(\text{rcp})} = 0.84$ at $c_s^{(\text{rcp})} = 0.64$ for the state of random close packing, and $b = 3.5$ for the power-law exponent. Derived from

fluidisation cell experiments, relation (2) applies to well-agitated granular dispersions. It may thus be expected to hold for dilute shear flows. When particles are densely packed, however, effects other than volume exclusion can contribute to the ordering of nearby grains and bias the roundness estimator. The particle shape may for instance play a role at high concentrations. This can be seen in the lower part of Fig. 6a, where the cylindrical particles are seen to orient their axes preferentially in the direction perpendicular to the flow. As such effects can lead to unreasonably high concentration values when the roundness estimate is used, a cap must be enforced at the maximum concentration $c_s^{(\max)} = 0.69$ evaluated from compaction tests (see Table 1).

In order to ascertain their range of validity, Larcher (2002) compared concentration measurements obtained using the above monoscopic technique with stereoscopic imaging measurements (Spinewine et al. 2003). For steady uniform granular-liquid flows similar to those of the present paper, the results obtained using the two techniques are in good agreement (difference less than 0.05 between the two estimates) for concentrations up to $c_s = 0.55$. As expected, however, the results diverge beyond this limit and only the stereo technique yields reasonable values for higher concentrations. Developed more recently and more complicated to apply, the stereo technique was not used for the present measurements, based exclusively on monoscopic images. As a result, the validity of the concentration measurements presented below is restricted to dilute and moderate concentrations ($c_s < 0.55$). Measurements in the high concentration range $0.55 < c_s < 0.7$ are documented for completeness, but a gray band will be used to highlight their uncertainty on the corresponding figures.

The typical data set for a single experimental run includes on the order of 100,000 velocity

vectors (see Fig. 7) and cell roundness measurements. This is one order of magnitude higher than the 10,000 measurements identified by Louge and Jenkins (1997) as the minimum size needed to obtain statistically meaningful vertical profiles of granular temperature. Such large sample sizes are similar to those generated by computer simulations, and the same statistical techniques (e.g. Allen & Tildesley 1987; Rapaport 1995) are needed to extract useful information.

Binning is used to extract vertical profiles of velocity and concentration. The flow depth is subdivided into non-overlapping horizontal slices of thickness $\delta = 1$ to 2 particle diameters, into which measurements are distributed to obtain local averages (see Fig. 7). The average horizontal velocity \bar{u}_k within the k -th bin, for instance, is given by

$$\bar{u}_k = \bar{u}(y_k) = \frac{\sum_i I_i^{(n)}(k) u_i^{(n)}}{\sum_i I_i^{(n)}(k)}, \quad (3)$$

where y_k is the height of the centre of the k -th bin and $I_i^{(n)}(k)$ is an indicator function defined by

$$\begin{cases} I_i^{(n)}(k) = 1 & \text{if } y_k - \delta/2 \leq y_i^{(n)} < y_k + \delta/2 \\ I_i^{(n)}(k) = 0 & \text{otherwise.} \end{cases} \quad (4)$$

For the volumetric concentration, bin averages $\bar{\xi}_k$ are first obtained from roundness values $\xi_i^{(n)}$, then transformed into solid concentration values c_s using relation (2).

Since some of the runs present a certain degree of unsteadiness (see infra), we also estimated coarse-grained mean velocities $\bar{u}_k^{(l)}$, averaged over blocks of 10 successive image frames rather than the entire image sequence. Once these mean velocities are obtained, fluctuation velocities are estimated from

$$u_i'^{(n)} = u_i^{(n)} - \bar{u}_i^{(n)}, \quad (5)$$

where $\bar{u}_i^{(n)}$ is the mean velocity component taken at location $y_i^{(n)}$ and time $t^{(n)}$. Rather than simply using the average $\bar{u}_k^{(l)}$ of the corresponding bin k and block l , we estimate the $\bar{u}_i^{(n)}$ by bilinear interpolation between the $\bar{u}_k^{(l)}$. Interpolation in space is especially important because the product of the mean flow gradient by the bin thickness is of the same order of magnitude as the velocity fluctuations. Simply subtracting the local bin average would thus add a spurious gradient contribution to the actual fluctuations.

In a manner analogous to (3), one could now estimate the mean-squared velocity fluctuations from

$$\overline{u'^2}(y_k) = \frac{\sum_n \sum_i I_i^{(n)}(k) u_i'^{(n)2}}{\sum_n \sum_i I_i^{(n)}(k)} \quad (6)$$

(see for example Hsiau & Shieh 1999). This estimate is however sensitive to measurement errors due to the limited accuracy and finite frequency at which particle positions are sampled. Based on the full velocity autocovariance function $\langle u_i'^{(n)} u_i'^{(n+k)} \rangle$, we show in appendix how it is possible to compensate both errors and obtain a more reliable estimate. The mean-squared velocity fluctuations reported hereafter are all obtained using this novel correction procedure.

2.3. Flow regimes

Experimental runs can first be subdivided into solid bed and loose bed runs. Flows over solid bottom occur when the granular phase deforms at finite shear rates down to the fixed floor of the flume. Flows over loose beds, by contrast, occur when a static deposit forms underneath the moving granular-liquid layer (see Figure 1). Inside this loose granular deposit, shear rates decrease to zero before reaching the flume floor. The thickness of the deposit is not predetermined, but adjusts to the flow through erosion or accretion until a state of dynamic

equilibrium is reached (Egashira *et al.* 2001). Intermediate conditions can also be observed, in which the flowing layer is in contact with the solid floor in the central portion of the flume (as seen through the port-hole) while static deposits line the corners between the floor and sidewalls. Ancey (2002) documented a similar situation for dry granular flows. To avoid unnecessary complications, test runs in which this hybrid situation was encountered are not included in the present data set.

The macroscopic behaviour of the experimental flows can be described using three non-dimensional parameters: (i) the inclination angle of the channel β ; (ii) the volumetric transport concentration $C_s = Q_s / Q$ where Q_s is the solid discharge and Q the total discharge (grains + water); (iii) the Froude number

$$Fr = \frac{U}{\sqrt{gH}}, \quad (7)$$

where H is the thickness of the flow layer (not including the static deposit), U is the depth-averaged velocity of the flow, and g is the gravitational acceleration. The transport concentration can be measured in two different ways: first, as the ratio $C_s^{(\text{bulk})} = Q_s^{(\text{bulk})} / Q^{(\text{bulk})}$ of solid to total discharge measured in bulk at the flume outlet; secondly, by integrating the sidewall imaging measurements over depth according to

$$C_s^{(\text{imag})} = \frac{q_s^{(\text{imag})}}{q^{(\text{imag})}} = \frac{\int_{y^{(\min)}}^{y^{(\max)}} c_s \bar{u} dy}{\int_{y^{(\min)}}^{y^{(\max)}} (c_s + c_w) \bar{u} dy}, \quad (8)$$

where $y^{(\min)}$ and $y^{(\max)}$ are lower and upper limits of the imaging window, q_s and q are respectively solid and total discharges per unit width, c_w is the water content ($= 1 - c_s$ wherever the granular phase is saturated with water). Here the mean velocity of water is assumed to coincide with the mean velocity \bar{u} of the grains. Based on the permeability measurements of Fig. 4, the specific discharge due to relative motion between the water and

the grains was computed for all runs. It was checked to amount to no more than 10 % of the corresponding total discharge.

For solid bed runs, the depth H can be measured manually as the height of the flow free surface above the flume bottom, then the mean velocity estimated from $U = Q^{(\text{bulk})} / BH$ where B is the channel width (20 cm). For loose bed runs, the thickness of the flow layer is more difficult to estimate since the boundary between moving and motionless grains is not sharply defined (see e.g. Fig. 6). Precise definitions of H and U can nonetheless be introduced based on depth-averaged momentum and kinetic energy:

$$(C_s \rho_s + (1 - C_s) \rho_w) H U = \Pi = \int_{y^{(\min)}}^{y^{(\max)}} (c_s \rho_s + c_w \rho_w) \bar{u} dy, \quad (9)$$

$$(C_s \rho_s + (1 - C_s) \rho_w) \frac{H U^2}{2} = K = \int_{y^{(\min)}}^{y^{(\max)}} (c_s \rho_s + c_w \rho_w) \frac{\bar{u}^2}{2} dy, \quad (10)$$

where Π and K are the depth-integrated momentum and kinetic energy per unit bed surface, and ρ_s and ρ_w are the densities of the granular material and water, respectively. In all three definitions (8), (9) and (10), the integration limits $y^{(\min)}$ and $y^{(\max)}$ do not need to correspond to any physically meaningful boundary. In effect, material contributions are weighted according to their participation in the flow motion, as measured by the local mean velocity \bar{u} . Estimates (9) and (10) are inspired from analogous treatments of boundary layers (e.g. Liggett 1994) and turbidity currents (Parker 2000). When detailed imaging measurements are available, they are also applicable to the solid bed runs.

The above macroscopic parameters can now be used to contrast the different flow regimes. A plot of Froude number Fr versus channel inclination β is first given on Fig. 8. Very different trends are observed depending on the state of motion along the floor of the flume. For the solid bed runs, the Froude number grows with increasing channel inclination. This is in accordance with intuitive expectations for open-channel flows. For the loose bed runs, by

contrast, the Froude number decreases as the channel becomes steeper! This apparent paradox can be understood by examining the role of the granular concentration. In the solid bed case, the inclination is assigned and the transport concentration (adjusted by altering the solid-liquid ratio inside the flume) affects only moderately the flow behaviour. As shown in Fig. 8, flows with a high transport concentration (in the range $C_s = 0.53 - 0.55$) are somewhat slower than flows with a low transport concentration (in the range $C_s = 0.51 - 0.53$), due to the contribution of the granular phase to the flow resistance. The impact of concentration on the Froude number is limited, however, because the flow depth is constrained by the solid bottom.

The situation in the loose bed case is quite different. First, the slope is no longer predetermined, but becomes coupled with the transport concentration. The flowing layer must find an equilibrium with the underlying static bed, reached when the flow neither erodes nor accretes the loose deposit. For a given transport concentration, there is a unique inclination at which this uniform, equilibrated state is obtained. Figure 9 shows the resulting relationship between slope and transport concentration: overall, higher solid to liquid ratios are needed to achieve balance when the inclination steepens. The influence of these higher solid concentrations on the flow rheology leads to slower flows. Furthermore, the thickness of the flowing layer also adjusts to the flow conditions: thicker flowing layers are obtained for steeper inclinations. The slower, thicker flows obtained on steeper slopes are thus characterised by significantly reduced Froude numbers, as illustrated on Fig. 8.

The loose bed data plotted on Figures 8 and 9 exhibit a rather sharp break of trend at a channel inclination of around 8 degrees. This corresponds to a transition of the flow from oversaturated to undersaturated conditions. Below an inclination of 8 degrees, water more than saturates the entire granular layer: a clear water layer flows over a fluid-driven sheet of

granular material supported by contacts with the stagnant bed. This regime is called *immature flow* in the debris flow literature (Takahashi 1991), and *sheet-flow* in the context of coastal sediment transport (see e.g. Jenkins & Hanes 1998). Above 8 degrees, by contrast, water does not saturate the whole moving layer: a partially emerged assembly of grains translates rigidly over a liquid-granular shear layer. This is the so-called *plug flow* regime. The intermediate state, or *mature flow* regime, features a saturated moving layer, composed throughout of a mixture of liquid and grains. The transport concentration at which full saturation occurs lies around $C_s = 0.5$.

As schematised on Fig. 10, four main regimes of interest can thus be distinguished: (a) loose bed, immature sheet-flow; (b) loose bed, mature flow; (c) loose bed, plug flow; and (d) solid bed flow. A more complete typology would include hybrid flow states featuring mixed loose-solid bed conditions across the flume width, and would further differentiate basal shear flows according to the degree of saturation. In the present work, we do not pursue such refinements and concentrate our attention on the micromechanics of loose bed flows. The ensuing analysis will thus focus on loose bed cases (a) to (c), with the solid bed case (d) examined for comparison purposes. Over solid beds, we restrict our attention to flows which are close to full saturation. Out of a catalogue of more than 100 experiments, 4 runs of each type are chosen for detailed imaging analysis. These 16 runs and their properties are listed in Table 2.

2.4. Steady uniform, planar flow approximation

Throughout our physical interpretation of the imaging measurements, we will assume that the observed mean flow field is steady in time, uniform in the longitudinal direction, and homogeneous in the transverse direction. Variations along the direction normal to the bed will be the only ones considered, greatly simplifying the picture. In particular, the stress state

within the flow can then be deduced from simple equilibrium considerations. Here we present various checks that were made to verify and qualify this idealisation.

As illustrated on Fig. 7b, the steady uniform character of the flow can be ascertained by examining mean velocity profiles averaged over separate time intervals (here 10 successive intervals of 1/10 the total footage duration for run 085). The longitudinal velocity profiles fluctuate within a certain range, but indicate no systematic drift that would indicate a sustained acceleration or deceleration of the flow. Plotted on the same Fig. 7b, normal-to-bed velocity profiles fluctuate likewise around their long term average, but the latter is very close to zero. If the average flow was not longitudinally uniform, converging or diverging streamlines would lead to non-zero mean velocities normal to the bed. Similar profiles are obtained for the other runs, although some of them feature stronger fluctuations.

To document the strength and nature of these fluctuations, Figure 11 presents time histories of the observed kinetic energy for representative flows of each of the four types. Here the specific kinetic energy is defined as

$$E(t^{(n)}) = \frac{1}{2} \sum_i (u_i^{(n)2} + v_i^{(n)2}) \quad (11)$$

i.e. the sum of the kinetic energies of the particles observed inside the imaging window at any given time $t^{(n)}$, divided by particle mass. This indicator was proposed by Campbell (1989) to verify steady state in the context of granular dynamics simulations. It is verified that, aside from some fluctuations, the specific kinetic energy remains steady over the measurement time frame. Some low frequency pulsations are nonetheless observed for the solid bed runs. Among all the tests, run no. 46 had the highest Froude number ($Fr = 3.2$) and exhibited the strongest free surface fluctuations (see Fig. 11a). This run also made clear the source of the unsteady behaviour: roll wave instability of the steep flows. In-phase variations of velocity

and depth are a characteristic signature of roll waves. As shown on Fig. 12, this feature shows up particularly vividly on a plot of specific kinetic energy E versus specific potential energy P of the observed particles, where the latter is estimated at any given time $t^{(n)}$ from

$$P(t^{(n)}) = g \sum_i y_i^{(n)}. \quad (12)$$

Even for the most extreme case, however, the pulsations are moderate and superposed onto a recognisable steady state. This is possibly because the channel is too short for roll wave coarsening to develop (Chang *et al.* 2000). Similar free surface instabilities have been observed for chute flows of dry granular materials (Prasad *et al.* 2000; Louge & Keast 2001). For flows over loose beds (Fig. 11b), steady state is closely approximated, except for some pulsations observed for the immature flow runs. Froude numbers greater than 3 for run 46 and greater than 1 for run 85 lie within the range of possible occurrence of rollwaves and antidunes, respectively.

The assumption that the flow is homogeneous in the transverse direction is most subject to caution. Three different means can be used to ascertain departures from this assumption: 1) measurements of free surface velocities across the channel width; 2) observations of the state of motion at the bottom boundary through the flume floor porthole; 3) comparison of depth-integrated side-wall measurements with bulk volumetric measurements made at the flume outlet. Measurements of free surface velocities imaged from the top yield nearly flat velocity profiles across the width, indicating a high degree of transverse uniformity. This is illustrated on Fig. 13a-b for run 41, and similar results were obtained for earlier runs over both solid and loose beds. It would be tempting to assume that this high degree of transverse uniformity recorded at the free surface applies as well to the flow interior, but this is not the case. Bottom observations through the flume floor porthole show that the state of motion at the flume centreline can be quite different from the motion close to the sidewall. For cases in

which hybrid loose-solid bed conditions occurred, a static layer having a thickness of up to 6 cm could be observed at the sidewall while the lowermost grains at the centre of the channel were still moving (as seen through the bottom porthole). Thus corner effects appear to endow the flow with a significant three-dimensional character at the base of the moving layer. Similar features have been documented by Spence and Guymer (1997) and Ancey (2002).

A further clear indication of transverse non-uniformity is provided by the discharge measurements. The total volumetric discharge $Q^{(\text{bulk})}$ measured at the outlet provides a reference value. On the other hand, an indirect estimate can be obtained by extrapolating sidewall imaging measurements to the whole flume width B . This estimated discharge is given by $Q^{(\text{imag})} = q^{(\text{imag})}B$, where $q^{(\text{imag})}$ is the depth-integrated flux defined in eq. (8). Figure 14 plots the measured values of $Q^{(\text{imag})}$ and $Q^{(\text{bulk})}$ against each other. For transversely uniform flows, one would expect $Q^{(\text{imag})} \approx Q^{(\text{bulk})}$. Instead, the sidewall imaging estimate $Q^{(\text{imag})}$ is found to underestimate the total discharge $Q^{(\text{bulk})}$ by some 30 %. This represents a much greater discrepancy than would be anticipated based on free-surface velocity data alone, which underlines that departures from uniformity become more severe towards the bottom.

Although measurements of the longitudinal velocity inside the flow are not available, it is possible to reconstruct a hypothetical velocity distribution which fits the above observations. The paraboloid surface illustrated on Fig. 13c was tuned to roughly match the observed pattern of motion along the top, side and bottom in a typical loose bed run. For this reconstruction as in the experiments, the apparent sidewall discharge is 30 % lower than the true total discharge. To check that the planar flow approximation remains reasonable despite such deviations from transverse uniformity, force balance considerations will be required. This will be addressed in the next section.

Even if sidewall measurements underestimate the overall flow rate, they may still reliably capture local flow properties such as the solid concentration and the granular temperature. The sidewall estimates of transport concentration, for instance, are in relatively good agreement with bulk outlet measurements, as shown on Fig. 14b. The exceptions are the dense plug flow runs (data circled on Fig. 14b), but the large discrepancies for these data are likely due to the measurement technique (the pattern-based concentration estimate breaks down in the dense limit) rather than to sidewall effects. Using computer simulations, Louge and Jenkins (1997) checked that the granular temperature is not strongly affected by the presence of a smooth sidewall. At least for rapid flow conditions, a good correspondence between near wall and interior flow states should thus be obtained.

3. Measured profiles and stress estimation

3.1. Depth profiles

Measured depth profiles for the four different flow regimes are plotted on Figures 15 to 18. On these and all subsequent figures, data points from a specific run are assigned a unique symbol shape. A legend documenting the correspondence between runs and symbols is included in Table 2. For a given run, filled and hollow symbols are used to denote data for which the predominant behaviour is ascertained to be either frictional or collisional, respectively. This distinction is made according to a criterion which will be introduced later in the analysis. On Figures 15-18, four panels are used to plot the following quantities: longitudinal velocity \bar{u} , granular concentration c_s , shear rate $\dot{\gamma} = \partial\bar{u}/\partial y$, and root-mean-squared fluctuation velocity $T^{1/2} = \sqrt{\frac{1}{2}\langle u'^2 + v'^2 \rangle}$. For three-dimensional granular flows, the granular temperature T is defined as $T = \frac{1}{3}\langle u'^2 + v'^2 + w'^2 \rangle$, however the third

component of velocity w is not measured in the present experiments, hence the rms fluctuation velocity is given instead as the square root of $T = \frac{1}{2} \langle u'^2 + v'^2 \rangle$.

The plots are made dimensionless using a combination of depth-averaged and viscous scales. First, depth-averaged quantities H and U are used to normalise the depth axis y and the mean velocity \bar{u} . Secondly, to obtain dimensionless descriptors of the shear rate and fluctuation velocity, we define the two Stokes numbers

$$St = \frac{1}{18} \frac{\rho_s}{\rho_w} \frac{d^2 \dot{\gamma}}{\nu_w} \quad \text{and} \quad St' = \frac{1}{18} \frac{\rho_s}{\rho_w} \frac{dT^{1/2}}{\nu_w} \quad (13a,b)$$

where ν_w is the kinematic viscosity of the liquid, and d the particle size. Let a particle move at velocity V with respect to the surrounding liquid. The Stokes number represents the ratio of two time scales: the time scale $\frac{1}{18} \rho_s d^2 / \mu_w$ of deceleration due to the Stokes viscous drag force $3\pi\mu_w dV$, and the time d/V needed for a particle to move a distance of one diameter through the liquid. Expressions (13a) and (13b) result from choosing as representative velocity V either the relative velocity $d\dot{\gamma}$ between adjacent sheared rows of particles, or the fluctuation velocity $T^{1/2}$.

This hybrid choice of dimensionless parameters is motivated by the following considerations. First, the mean velocity profiles are normalised using depth-averaged variables in order to highlight the high degree of macroscopic similarity between different test runs corresponding to the same flow type. As shown on panel (a) of each of the Figures 15-18, the mean velocity profiles collapse onto well-defined curves for each of the flow regimes. On the other hand,

normalising the shear rates and granular temperature data by their depth-integrated values would obscure the flow rheology. Dimensionless Stokes numbers are therefore used instead on panels c-d of Figures 15-18. Because all runs of our experiments involve the same granular material and liquid, these dimensionless numbers are not strictly necessary to compare measurements within the present dataset. In fact, each of the two Stokes numbers (13a) and (13b) includes either $\dot{\gamma}$ or $T^{1/2}$ as the single variable quantity. Stokes numbers are adopted nonetheless to facilitate comparisons with data obtained by other investigators for different solid particles and liquids. To highlight the fact that both dimensionless and dimensional representations are equivalent for variables $\dot{\gamma}$ and $T^{1/2}$, scales are given in dimensional units as well on panels (c) and (d) of Figures 15-18.

The various profiles bring out the characteristics of each flow regime. For the sheet-flow runs (Fig. 15), the mean velocity profiles (panel a) are convex, with maximum shear rates (panel c) observed in a sub-layer close to the free-surface. The solid concentration (panel b) evolves monotonously over depth, with maximum values in the closely packed bed and very small values close to the free surface. The concentration profiles are close to linear in the flowing region, in accordance with the observations of Shook *et al.* (1982). Unlike the kinetic theory computations of Jenkins and Hanes (1998) and Hsu *et al.* (2004), the present results do not exhibit any conspicuous “shoulder” region of constant concentration within the flowing layer. Finally the fluctuation velocity profiles of panel (d) present an interesting region of nearly constant values spanning much of the flow depth, with decaying values in the vicinity of the

bed. Such a region of constant fluctuation velocity at the top of the sheet-flow layer was predicted by the computations of Jenkins and Hanes (1998; see also Hsu *et al.* 2004).

For the mature flow runs (Fig. 16), the maximum shear rate occurs at mid-depth, where a change of concavity of the mean velocity profile occurs (see Fig. 16a,c). The velocity profile is close to linear over much of the shear layer depth, tapering off at the top and bottom. Comparison of panels (c) and (d) of Fig. 16 shows that the shear rate and fluctuation velocity profiles are similar to each other over much of the flow depth. The most significant departure from similarity occurs at the top of the flow, where the shear rate approaches zero but the fluctuation velocity reaches a new maximum. A similar inflection near the free surface was observed by Silbert *et al.* (2001) in their simulations of dry granular flows on a rough incline, without any lateral boundary. In the present case, however, this effect seems to be associated with stick-slip motion of partially emerged, but wet particles adhering intermittently to the flume sidewall. Images filmed from the side show these motions clearly. On the other hand, footage filmed from above indicates that the free surface fluctuation velocities are much lower away from the side wall. The high fluctuation velocity measured here at the top thus appears to be an artefact due to the lateral boundary.

As seen on Fig. 17, the plug flow runs feature a mid-depth shear layer comprised between two nearly rigid blocks of densely packed grains. The plug layer at the top translates at constant velocity, while the loose bed stays motionless at the bottom (see Fig. 17a). The corresponding

shear rate and fluctuation velocity profiles (Fig. 17c,d) have a Gaussian-like shape with values reaching a maximum in the middle of the shear layer, and decreasing to zero in both the overlying plug and underlying bed. The shear rate and fluctuation velocity curves are seen to present a very high degree of similarity. On panel 17b, pattern-based solid concentration measurements are seen to break down for the dense plug flow runs. This is indicated by the flat profiles capped at the maximum admissible value $c_s^{(\max)} = 0.69$.

For the above three regimes, the flows find an equilibrium with the erodible static bed. The lowermost parts of the curves of Figures 15-17 (panels a, b, and c) are very similar: they asymptotically connect to a state of no motion at the bottom. As shown on Fig. 18, profiles for the solid bed flows are quite different. The maximum shear rates are observed at the bottom of the layer, close to the flume floor, rather than at the top or at mid-depth (Fig. 18a,c). Solid concentrations are minimum close to bottom (Fig. 18b). Finally, the fluctuation velocity (and hence the granular temperature) is maximum at the base of the flowing layer (Fig. 18d). Very different from the loose bed results of Fig. 15-17, the present solid bed measurements are similar to computed profiles derived from discrete particle simulations of dry granular flows (Campbell 1990, Silbert et al. 2001).

For further observations regarding the global behaviour of the different flow regimes, the reader is referred to Armanini *et al.* (2000) and Larcher (2002). Our purpose for the remainder of the present analysis is to probe the flow behaviour on the local scale. Specifically, our aim

is to examine the rheology of the flow: relate the local stress state to the local concentration and motions of the liquid-bathed solid grains. Preliminary findings from this effort were reported in Capart *et al.* (2000).

3.2. Estimation of the granular stresses

Assuming that the flows are steady, uniform, and planar, granular stresses can be determined based on force balance in directions normal and parallel to the bed. In the present section, the procedure adopted to estimate the stresses is first explained. The procedure does not take into account non-equilibrium pore pressures or friction along the side walls. These effects will then be examined to check that their influence on the results is limited.

In order to determine the granular stresses, both the solid and liquid concentrations must be known over the flow depth. The imaging measurements yield solid concentration profiles $c_s(y)$. The water concentration profiles $c_w(y)$ are then estimated as follows. Below the saturation line y_w (identified by visual inspection of the video images), the water content is simply $c_w = 1 - c_s$. Above the saturation line, on the other hand, it is set to the value $c_w = S_r = 0.08$ of the specific retention (see Table 1). Assuming that the flow is planar and steady uniform, the shear stress $\tau(y)$ at a given level y balances the longitudinal component of the overlying weight according to

$$\tau(y) = \int_y^{y_{\text{max}}} (c_s(y)\rho_s + c_w(y)\rho_w)g \sin\beta \, dy. \quad (14)$$

where β is the inclination of the flow with respect to the horizontal. Likewise the total

normal stress $\sigma(y)$ at level y balances the normal component of the overlying weight

$$\sigma(y) = \int_y^{y_{\max}} (c_s(y)\rho_s + c_w(y)\rho_w)g \cos\beta dy. \quad (15)$$

To obtain the effective normal stress representing the contribution of granular contacts, one must then subtract the pore water pressure

$$\sigma' = \sigma - p_w. \quad (16)$$

When the entire granular layer is submerged and saturated with water, the pore water pressure is simply $p_w = \rho_w g(y_w - y) \cos\beta$, where y_w is the water surface level. The effective normal stress is then

$$\sigma' = \int_y^{y_w} c_s(y)(\rho_s - \rho_w)g \cos\beta dy. \quad (17)$$

which balances the submerged weight of the overlying grains. On the other hand, when the top of the granular layer de-saturates and partly emerges above the water level y_w , the pore pressure at level $y < y_w$ becomes

$$p_w = \rho_w g(y_w - y) \cos\beta - \rho_w g h_c. \quad (18)$$

where h_c = height of capillary rise. Upon partial de-saturation, the full weight of the emerged grains, the retained water, and the weight of the capillary water must be supported by granular contacts underneath (see e.g. Das 1990). Capillary rise was observed for a partially emerged plug flow run by connecting at position x_p a piezometric tube of large diameter to the sidewall of the flume. The height of capillary rise h_c was then measured during flow as the difference in elevation $z_w(x_p) - z_p$ between the saturation line and the water level in the tube. The height obtained in this fashion was found to lie between 5 and 6 mm, corresponding to the lower end of the range measured in static tests (see Table 1). A value $h_c = 5$ mm is

retained for the present calculations.

Two important assumptions made in the above analysis need to be critically examined. First, pore pressures p_w are assumed to be hydrostatic. Non-equilibrium pore pressures associated with volumetric expansion or contraction of the granular phase are thus neglected. These effects are known to be important for unsteady debris surges in which the granular matrix has a low permeability (Iverson 1997; Major & Iverson 1999). They are however expected to be very limited in the present experiments involving steady uniform flow of coarse grains and a low-viscosity liquid. A time scale for pore-pressure relaxation can be estimated as (Spence & Guymer 1997)

$$t_{\text{relax}} = \frac{\rho_w}{\rho_s - \rho_w} \frac{c_b - \bar{c}_s}{c_b \bar{c}_s} \frac{H}{k} \quad (19)$$

where H is the depth of the flowing liquid-granular layer, k and \bar{c}_s are respectively the permeability and average solid concentration in this flowing layer, and c_b is the solid concentration in the resedimented static bed. A corresponding length scale is given by $\ell_{\text{relax}} = Ut_{\text{relax}}$ where U is the mean velocity of the flowing layer. For the present experiments, representative values are (see Tables 1 and 2) $\rho_s / \rho_w = 1.54$, $\bar{c}_s = 0.5$, $k = 7 \text{ cm/s}$, $c_b = 0.6$, $H = 8 \text{ cm}$ and $U = 30 \text{ cm/s}$. Pore pressure relaxation effects can therefore be expected to act on scales of the order of $t_{\text{relax}} = 0.6 \text{ s}$ and $\ell_{\text{relax}} = 20 \text{ cm}$, whereas our experimental flows are allowed to develop on time scales of some ten seconds and length scales of a few meters. This appears to be more than enough for pore pressure to equilibrate over the depth and attain the hydrostatic values corresponding to steady uniform conditions.

A second important assumption is that forces due to the sidewalls can be neglected in the longitudinal force balance. For dry granular flows over self-forming stationary heaps in channels of finite width, Taberlet et al. (2003) found that lateral friction effects could play a strong role. Those experiments, however, concern thin channels for which the width W is small in proportion to both the grain diameter d ($W/d \sim 10$) and flow depth H ($W/H = 2/3$ to 2). In the present experiments, the width to diameter ratio W/d is around 70, hence arching effects should be weaker. Runs classified as sheet-flow and mature are also characterised by higher aspect ratios $W/H = 3$ to 10. For these runs, it appears reasonable to neglect the effect of lateral friction compared to the influence, say, of the liquid content, which plays a key role in our experiments.

This can be checked by looking at the macroscopic force balance for these runs (Takahashi 1991; Armanini et al. 2000). Consider a flowing layer of grains over a loose slope of inclination β , fully saturated with water, having thickness H and average solid concentration \bar{c}_s assumed to coincide with the transport concentration C_s . At the base of the layer, frictional conditions apply, and we expect a Coulomb-Terzaghi relationship between shear stress and effective normal stress

$$\tau = \tan \theta_c \sigma' \quad (20)$$

where $\theta_c = 31^\circ$ is the critical friction angle derived from the simple shear tests (see Table 1).

On the other hand, assuming steady uniform conditions, shear and normal effective stresses

can be estimated by balancing forces applied to the flowing layer. Neglecting friction along lateral walls, the forces involved are the pull of gravity and stresses along the base. Hydrostatic pore pressures are also assumed. The resulting expressions are

$$\tau = [\rho_w + (\rho_s - \rho_w)C_s]gH \sin\beta \quad (21)$$

$$\sigma' = (\rho_s - \rho_w)C_s gH \cos\beta \quad (22)$$

Substitution into the Coulomb-Terzaghi expression yields a relationship between the inclination β and the transport concentration C_s :

$$\tan\beta = \frac{(\rho_s - \rho_w)C_s}{\rho_w + (\rho_s - \rho_w)C_s} \tan\theta_c. \quad (23)$$

The resulting curve is plotted on Fig. 9 against the measured data. Good agreement is found up to an inclination $\beta = 8$ degrees. This is the slope beyond which a plug flow regime is observed, and the relationship no longer applies because part of the moving granular layer desaturates. At least for the sheet-flow and mature runs, a macroscopic force balance conducted by neglecting side wall and non-equilibrium pore pressure contributions is thus found to be consistent with the observations.

For the plug flows, the ratio W/H drops to 2 and below. Also, partial desaturation of the granular layer changes the nature of the contacts between the grains and the walls. A stronger influence of the sidewalls on the force balance can therefore be expected. This influence could be estimated if measurements were available for various flume widths (as in Taberlet *et al.* 2003). Unfortunately, such experiments were not performed, and sidewall effects had to be neglected even for the plug flow runs.

4. Rheological interpretation

Subject to the limitations highlighted above, the present experiments yield measurements of mean velocity, fluctuation velocity, and solid concentration as well as estimates of shear and normal stresses. The uniform flow flume thus provides sufficient information to serve as a rheometer. The present section now seeks to exploit this information to construct an interpretation of the flow structure.

4.1. Transition between frictional and collisional behaviours

The relationship between stress and shear rate can first be examined in light of the ideas proposed by Bagnold (1954). To describe the stresses induced by shearing a liquid-saturated granular dispersion, Bagnold introduced a non-dimensional shear rate defined as

$$Ba = \frac{\rho_s \lambda^{1/2} d^2}{\mu_w} \dot{\gamma}, \quad (24)$$

subsequently called the Bagnold number by Hill (1966). Aside from the absent numerical factor 1/18, the Bagnold number Ba differs from the Stokes number St defined earlier only by the presence of a non-dimensional factor λ called the linear concentration. This factor was introduced by Bagnold to account for the effect of solid concentration c_s and is defined as

$$\lambda(c_s) = \frac{1}{(c_{s0}/c_s)^{1/3} - 1}, \quad (25)$$

where $c_{s0} = 0.74$ is the solid concentration corresponding to a crystalline close packing of equal spheres. He further introduced non-dimensional shear and effective normal stresses

$$\frac{\tau}{\mu_w^2 \lambda / (\rho_s d^2)} \quad \text{and} \quad \frac{\sigma'}{\mu_w^2 \lambda / (\rho_s d^2)}. \quad (26a,b)$$

The term *dispersive stress* was used by Bagnold to refer to the rate-dependent collisional normal stress observed in his experiments. Here we retain the more general term *effective normal stress* used in soil mechanics to describe the normal stress associated with particle interactions regardless of the nature of these interactions. On Figures 19-21, we use these quantities to characterise the relationship between stresses and shear rate observed in the present experiments. Figures 19, 20, and 21 respectively show the dimensionless shear stress, dimensionless normal stress, and stress ratio τ/σ' over the full range of Bagnold numbers Ba covered by the flow profiles of Figures 15-18.

Based on his experiments performed with neutrally buoyant wax particles bathed in either water or a glycerin-water-alcohol mixture, Bagnold identified two different rheological behaviours: a macro-viscous regime (for $Ba < 40$) characterised by a linear relation $\tau \propto \dot{\gamma}^1$ between stress and shear rate, and a grain-inertia regime (for $Ba > 450$) where stresses vary as the square of the shear rate $\tau \propto \dot{\gamma}^2$. On the log-log plots of Fig. 19 and 20, these relationships correspond to straight lines with inclinations 1 and 2, respectively. For the present experiments performed with particles heavier than the surrounding liquid ($\rho_s / \rho_w = 1.57$), the data suggest a different picture. For large Bagnold numbers ($Ba > 1000$), measurements are indeed consistent with a quadratic relation $\tau \propto \dot{\gamma}^2$ between shear stress and shear rate, corresponding to Bagnold's inertial regime. However for lower Bagnold numbers (slower rates of deformation), the data do not switch to a linear relationship, but to a band of roughly zero slope $\tau \propto \dot{\gamma}^0$ implying approximately rate-independent shear stresses.

Turning our attention to the stress ratio τ/σ' (Fig. 21), Bagnold suggested constant values $\tau/\sigma' \approx 0.75$ and $\tau/\sigma' \approx 0.32$ applicable to the macro-viscous and grain-inertia regimes, respectively. Here again a different behaviour is recorded in the present experiments. For slow deformation, the data do cluster around a roughly constant stress ratio. The level of this stress ratio further appears reasonably well approximated by the value $\tan 31^\circ = 0.6$ applicable at steady state to the very slow deformation rates of the simple shear tests (see Table 1). This correspondence is observed despite the fact that the stresses applied in the simple shear tests have a much greater magnitude than those experienced in the channel.

For larger Bagnold numbers, however, stress ratios do not lock onto another constant value. While both the shear and normal stress vary roughly quadratically with the shear rate, their precise ratio is neither constant nor dependent solely on the shear rate. Rather, measurements for differing flow conditions diverge from each other in a way that indicates that an important degree of freedom is missed. For dry granular flows, kinetic theories hold that the extra variable which is involved is the granular temperature, a measure of the intensity of velocity fluctuations. These fluctuations are likewise expected to play a role when rapidly sheared grains are bathed in a liquid. Thus our rapid shear data are consistent with a collision-dominated inertial regime, but the observed behaviour is not quite as simple as Bagnold's description would imply.

To summarise, for slow shear ($Ba < 1000$) the data present all the characteristics of Coulomb-type frictional behaviour: shear and normal stresses proportional to each other and at most weakly dependent on the rate of shear. For rapid deformation, on the other hand, the stresses scale quadratically with the shear rate in accordance with expectations for a collision-dominated inertial regime. Putting the pieces together, the data thus indicate a transition from frictional to inertial behaviour instead of the transition from macro-viscous to inertial behaviour identified by Bagnold. A sharp contrast between frictional and collisional behaviours was similarly observed by Aharonov and Sparks (1999) in their numerical simulations of sheared granular assemblies.

This frictional-collisional picture presents one puzzling feature. Nowhere does one observe the scaling $\tau \propto \mu_w \dot{\gamma}$ expected of a Newtonian-like macro-viscous fluid. In the frictional state, the shear and normal stresses relate to each other rather than to the rate of deformation. In the collisional state, on the other hand, the water viscosity μ_w drops out from the quadratic scaling

$$\frac{\sigma'}{\mu_w^2 \lambda / (\rho_s d^2)} \propto Ba^2 = \left(\frac{\rho_s \lambda^{1/2} d^2}{\mu_w} \right)^2 \dot{\gamma}^2. \quad (27)$$

Hence for both frictional and collisional states, the viscosity of the liquid plays no apparent role in controlling the stresses. And yet, the transition from frictional to collisional behaviour appears well-defined on Bagnold plots constructed on the basis of viscosity scalings. Specifically, the transition seems to occur around a Bagnold number $Ba^* \approx 1000$. This means that while the viscosity of the pore liquid controls neither the frictional nor the

collisional behaviour, it may determine the point at which the sheared mixture switches from one behaviour to the other. In other words the frictional-collisional transition could be controlled by viscous effects through a mechanism that remains to be elucidated.

At this point, we have not yet exploited the information provided by the direct measurements of granular temperature. We will now use these data to try to refine this emerging picture of the flow rheology.

4.2. Relationship between shear rate and fluctuation velocity

Figure 22 documents the observed relationship between shear rate $\dot{\gamma} = \partial\bar{u}/\partial y$ and square root of the granular temperature $T^{1/2}$. Both quantities are plotted in their dimensionless Stokes number forms St and St' defined in equations (13a,b). An alternative way to compare the mean rate of shear $\dot{\gamma} = \partial\bar{u}/\partial y$ with the intensity of the granular velocity fluctuations is to form the ratio

$$R = \frac{d\dot{\gamma}}{T^{1/2}} = \frac{St}{St'}, \quad (28)$$

a dimensionless parameter introduced by Savage and Jeffrey (1981). As discussed in Savage (1998) and Louge (2003), the parameter R is typically found to be of order unity in computer simulations of sheared granular media. Savage (2002, personal communication) even suggests that a constant value of $R \approx 0.8$ may characterise granular behaviour over a wide range of conditions, including rapid collisional flow and slow frictional deformation.

In the present experiments, shear rate and fluctuation velocity are indeed found to be approximately proportional to each other. Constant values of the Savage-Jeffrey parameter R plot as straight lines on Figure 22, and the data cluster in a sector that goes from $R = 1$ to $R = 2.5$. However the measured Stokes numbers St and St' do not lie on a straight line over their entire range of variation. Stokes numbers corresponding to slow deformation (roughly $St < 10$) evolve roughly in the one-to-one ratio

$$R = \frac{St}{St'} \approx 1. \quad (29)$$

Yet beyond values of $St \approx St' \approx 5 \div 10$, the data deviate from this straight line and eventually reach ratios as high as $R = 2.5$ for rapid shear rates. Here again, the data suggest a transition dependent upon the rate of shear. The Stokes number $St^* \approx 7.5$ at which the transition occurs corresponds to a shear rate $\dot{\gamma}^* \approx 6 \text{ s}^{-1}$ and to a fluctuation velocity $(T^{1/2})^* \approx 2.4 \text{ cm/s}$. This value of the Stokes number also matches the transitional Bagnold number $Ba^* \approx 1000$ identified earlier, if one adopts for the linear concentration λ the value $\lambda^{(\max)} \approx 40$ associated with a compact granular medium ($c_s = c_s^{(\max)} = 0.69$).

On both sides of the transitional Stokes number $St^* \approx 7.5$, the data trends are consistent with frictional and collisional behaviours, respectively. Under slow deformations, frictional stresses are transmitted through enduring contacts among solid particles. As they stay in close contact, neighbouring particles must undergo coordinated motions. Under such kinematic constraints, fluctuating and mean shear components of the granular flow must relate to each other. It is thus not surprising to find that in the limit of slow deformation, grain motions are

characterised by a constant Savage-Jeffrey parameter. For rapid collisional flow, by contrast, particles interact through short-lived contacts. The fluctuation energy and shear rate remain coupled through energy constraints, as the kinetic energy dissipated by random motions must be derived from the work of the mean shear. However the random motions of the particles are only loosely constrained by the motions of their neighbours, hence the fluctuation velocity and the shear rate must not remain locked in strict proportion to each other.

There are two other reasons to believe that Stokes numbers in the vicinity of $St^* \approx 7.5$ have a special significance. The first reason is microscopic, and has to do with the effect of the ambient fluid on collisions between individual grains. Various studies (Davis *et al.* 1986; Joseph *et al.* 2001; Gondret *et al.* 2002) have shown that particles immersed in a fluid bounce off each other in a way that is governed by the value of Stokes number

$$St_{\text{coll}} = \frac{1}{18} \frac{\rho_s}{\rho_w} \frac{d(2U_i)}{\nu_w} \quad (30)$$

where U_i is the particle speed before impact, measured relative to the collision plane (either the plane tangent to two particles at their point of contact or a rigid wall in the case of particle-wall collisions). At very high Stokes numbers ($St_{\text{coll}} > 1000$), particles rebound with a velocity U_r characterised by a coefficient of restitution $e = U_r / U_i$ close to the value applicable to dry collisions. For lower Stokes numbers, by contrast, the coefficient of restitution decreases under the influence of the viscous ambient fluid. Most dramatically, when the Stokes number falls below a critical value of about $St_{\text{coll}}^* \approx 10$, the elastic energy stored upon contact is entirely dissipated in the fluid and the coefficient of restitution drops to

zero. Particles no longer exhibit any rebound.

Drawn from experiments involving collisions of individual particles with a vertical wall (Joseph *et al.* 2001) or horizontal floor (Gondret *et al.* 2002), the above observations are consistent with the elastohydrodynamic analysis of Davis *et al.* (1986) and have also been found recently to account for a change in avalanche regime in rotating drum experiments (Courrech du Pont *et al.* 2003). They suggest a compelling microscopic interpretation of the change in behaviour observed in the present experiments in the vicinity of $St^* \approx 7.5$. Under rapid shear, particles are able to rebound upon colliding and thus interact through short-lived contacts. Under slower deformations, on the other hand, the shear-induced fluctuating motions are not strong enough for particles to rebound upon impact and take off from their enduring contacts with neighbouring grains. Under the influence of the viscous ambient fluid, therefore, inelastic collapse occurs at the transition.

The second reason to attach a special significance to the transitional Stokes number $St^* \approx 7.5$ lies in the observed macroscopic behaviour of the downslope flows. As discussed earlier, uniform flows over loose beds increase their solid-to-liquid ratio and decrease their velocity as flow inclinations become steeper. However, the experiments indicate that there is a clear limit to how slow the steep flows can become. This is documented on Figure 23, which plots maximum shear rates against flow inclination. The maximum shear rate $\dot{\gamma}_{\max} = (\partial \bar{u} / \partial y)_{\max}$ observed for a given run is defined as the maximum value taken by the shear rate over the

entire depth of the debris flow. It is made dimensionless by introducing the Stokes number

$$St_{\max} = \frac{1}{18} \frac{\rho_s}{\rho_w} \frac{d^2 \dot{\gamma}_{\max}}{\nu_w} \quad (31)$$

Rather than decreasing indefinitely as flow inclinations get steeper, the maximum shear rate is found to reach an asymptote

$$(St_{\max})_{\min} \approx 5 \approx St^* \quad (32)$$

where St_{\max} levels off to values close to the transitional Stokes number $St^* \approx 7.5$. The transitional Stokes number thus appears to set a *minimax* constraint on the downslope flow, determining a minimum value that must be attained by the maximum shear rate.

This suggests that for the slowest flows, the maximum shear rate $\dot{\gamma}_{\max}$ (observed for the plug flows at the core of their mid-depth shear layer) does not decrease below the minimum level necessary for viscous and/or collisional effects to retain control on the overall flow rate. If a slowly flowing layer exhibited purely frictional behaviour, then because frictional rheology is rate-independent there would be no constraint on the speed of deformation. By contrast, the emergence of a rate-dependent control somewhere in the flow (in this case in the middle of the shear layer) provides an internal boundary condition which can set the overall flow rate.

4.3. Rheological structure of the loose bed flows

Based on the above observations, the full set of measurements corresponding to the 16 detailed test runs documented on Figures 15-18 were tentatively split into two subsets. Data for which $St' < St^*$ form the first subset, and are assumed to represent predominantly

frictional behaviour. Data for which $St' > St^*$, on the other hand, are taken to represent predominantly collisional behaviour. On the various figures, data classified as frictional or collisional in this fashion are plotted as filled or hollow symbols, respectively. Admittedly, the choice of a precise cut-off at the value $St^* \approx 7.5$ is somewhat arbitrary. Nonetheless, the resulting binary scheme accounts rather well for the distinct trends documented on Figures 19 to 22.

The classification can now be used to examine the distribution of rheological behaviour over depth for the various loose bed flow regimes. When mapped back to the original profile data of Figures 15-18, the frictional-collisional classification organises the flow into separate sub-layers governed predominantly by one mechanism or the other. For the immature flow regime (Fig. 15), water-entrained grains are sheared sufficiently strongly to be characterised by collisional behaviour over most of the depth of the flowing layer. Frictional behaviour is relegated to a thin boundary layer separating the collisional sheet from the static underlying loose bed. This is consistent with the description of sheet-flow sediment transport proposed by Jenkins and Hanes (1998) and analysed recently in more detail by Hsu *et al.* (2004). At the other end of the range (Fig. 17), the plug-flow regime features relatively slow deformations and frictional behaviour over the entire depth, except for the core of the shear layer which lies close to the transition point between frictional and collisional behaviours. In between, the mature regime (Fig. 16) exhibits a composite structure in which a collisional layer of finite thickness is sandwiched between two frictional layers. Granular-liquid flows over loose bed

can thus be described as rheologically stratified flows, responding to changes of inclination and liquidity by modifying the extent of their frictional and collisional sub-layers.

4.4. Collisional stress functions

A final objective of the present rheological analysis is to examine more closely the collisional behaviour of the granular-liquid mixture. In accordance with our binary classification, this examination is restricted to measurements for which $St' > St^*$, the transitional Stokes number ascertained earlier to mark the approximate onset of collisional behaviour. Specifically, the aim of this subsection is to compare measurements in that range with both the original relations of Bagnold and the more recent predictions of kinetic theories.

The relationships between stresses and shear rate proposed by Bagnold (1954) on the basis of his neutral suspension experiments can be written

$$\sigma' = 0.042 \cos \alpha \lambda^2 \rho_s d^2 \dot{\gamma}^2 \quad (33)$$

$$\tau = 0.042 \sin \alpha \lambda^2 \rho_s d^2 \dot{\gamma}^2 \quad (34)$$

where $\tan \alpha = 0.32$ and $\lambda(c_s)$ is the function of granular concentration defined in eq. (25). The corresponding stresses predicted by kinetic theories of collisional granular flows involve the granular temperature T in addition to the shear rate $\dot{\gamma}$. Derived in analogy with the kinetic theory of dense gases (Chapman & Cowling 1970; Lun *et al.* 1984), the relationships can be written (Jenkins & Hanes 1998)

$$\sigma' = (1 + 4c_s g_0) c_s \rho_s T \quad (35)$$

$$\tau = \frac{8c_s g_0 E}{5\pi^{1/2}} c_s \rho_s d T^{1/2} \dot{\gamma} \quad (36)$$

where

$$E = 1 + \frac{\pi}{12} \left(1 + \frac{5}{8c_s g_0} \right)^2. \quad (37)$$

In the above relations, the function

$$g_0(c_s) = \frac{2 - c_s}{2(1 - c_s)^3} \quad (38)$$

describes the dependence of the rate of collisions between particles on the granular concentration c_s , and was derived by Carnahan and Starling (1969) from an approximate virial expansion.

The description of Bagnold and kinetic theory are similar in various regards. One can check first that the functional form of Bagnold's equations (33)-(34) is retrieved by assuming a constant value of the Savage-Jeffrey parameter $R = d\dot{\gamma}/T^{1/2}$ in relations (35)-(36). Through functions $\lambda(c_s)$ and $g_0(c_s)$, furthermore, both relations account for the highly nonlinear influence of the granular concentration c_s . A difference is that while the Bagnold relations are semi-empirical in nature, the kinetic relations follow from theory through a rigorous approximation procedure and involve no adjustable empirical constants. Their predictions have been validated to a great extent by 3D computational simulations (Campbell 1989). Predictions for 2D granular flows (monolayers of disks or spheres held between parallel plates) were further found to agree well with detailed experiments (Azanza *et al.* 1999). As he was the first to propose that granular shear and normal stresses could be quadratic in the shear rate, Bagnold himself can of course be credited for some of the achievements of the kinetic

theories.

Despite this success, the applicability of either or both of these descriptions to liquid-granular flows of the type examined in the present study is not a settled issue. First, Bagnold's 1954 experiments were performed with neutrally buoyant spheres in water ($\rho_s = \rho_w$) instead of particles denser than the ambient fluid. In addition, a recent re-analysis of the experimental device and results of Bagnold (Hunt *et al.* 2002) has cast some doubts on his conclusions. Kinetic theories of collisional granular flows, on the other hand, were originally derived for dry granular flows. While it was argued by Jenkins and Hanes (1998) that relations (35) and (36) could be applied to granular-liquid flows as well, this has not to date been checked against detailed measurements of granular motions.

Comparisons with the Bagnold relations are first presented. On Figures 24 and 25, ratios $\sigma' / [\rho_s d^2 \dot{\gamma}^2]$ and $\tau / [\rho_s d^2 \dot{\gamma}^2]$ are plotted as a function of granular concentration c_s . The measured data collapse reasonably well on both plots, with only moderate scatter. The curves representing the Bagnold stress functions (33) and (34), however, do not agree equally well with the corresponding measurements. On Fig. 24, the normal stress function of Bagnold is found to agree rather well with the data across the whole range of concentrations c_s . For the shear stress function (34) plotted on Fig. 25, however, the agreement is much less satisfactory: the shear stress ratio $\tau / [\rho_s d^2 \dot{\gamma}^2]$ is strongly underestimated at lower values of concentration. This stems from the fact that the present collisional flow measurements do not exhibit the

constant stress ratio τ/σ' assumed by Bagnold. While not consistent with Bagnold's analysis, this feature is nonetheless compatible with Bagnold's own measurements. In their recent re-assessment, Hunt *et al.* (2002) point out that the stress ratio in Bagnold's experiments was not constant but varied by as much as a factor of 3. A similar range of variation is observed in the present experiments (see Fig. 21).

In their re-assessment, Hunt *et al.* (2002) suggest that Bagnold's 1954 experimental findings could in fact be due to flaws in the design of his annular rheometer, rather than reflect actual collisional interactions between grains. In particular, they show that the shear stress dependence on the shear rate measured by Bagnold could just as well have been produced by a Newtonian fluid with a concentration-dependent viscosity undergoing boundary layer flow along the end plates of the annulus.

While we cannot rule out the alternative mechanism suggested by Hunt *et al.*, the present experiments do provide some support for Bagnold's original conclusions regarding the inertial regime. Our measurements of liquid-granular flow in a rectilinear flume exhibit behaviours close to those observed by Bagnold in his annular rheometer and attributed by him to collisional effects. Despite the quantitative deviations, Bagnold's shear stress relation does match the qualitative data trend recorded in the present experiments. Most strikingly, the normal stress relation proposed by Bagnold to fit his data agrees quite well with our new measurements. Since the alternative mechanism of Hunt *et al.* can account for the shear

stresses but not for the normal stresses observed by Bagnold, we feel that Bagnold's original interpretation in terms of granular collisions remains compelling.

Comparisons with kinetic theory predictions are presented on Figures 26 and 27. Here the measured ratios $\sigma' / [c_s \rho_s T]$ and $\tau / [c_s \rho_s d \dot{\gamma} T^{1/2}]$ are plotted as a function of concentration, together with solid lines denoting the kinetic functions (35) and (36). Unlike the Bagnold relations, the stress functions derived from kinetic theory are found to underestimate both the normal and shear stresses. Since computational and experimental data for dry granular flow have been found to confirm the predictions of kinetic theories, we tentatively attribute this discrepancy to the presence of a dense interstitial liquid in our experiments.

More specifically, we surmise that added mass effects are largely responsible for the underestimation of the normal and shear stresses recorded in Figures 26 and 27. For particles to move about within the two-phase mixture, conjugate motions of the surrounding water are required. In particular, abrupt changes in granular velocities associated with inter-particle impacts must be associated with pressure impulses and sudden accelerations of the pore water. The resulting dynamic coupling between the particles and the liquid can be described as an added mass contributing to particle inertia.

Such added mass effects play a key role in bubbly flows (Russo & Smereka 1996; Kang *et al.* 1997), where the apparent inertia of the massless bubbles is entirely due to the embedding

liquid. While not quite as prevalent, they should likewise be expected to play a role in liquid-granular flows, where the density of the interstitial fluid is of the same order as the density of the particles. This was verified by Zenit *et al.* (1997, 1998), who documented experimentally the water pressure impulses induced by submerged collisions of particles with each other and with walls.

A quantitative estimate of the added mass effect in the present flows is derived in the following way. First, the added mass associated with random particle motions is estimated in the way suggested by Zuber (1964; see Batchelor 1988). It is assumed that a single particle accelerates in an environment constrained by neighbouring motionless particles, with the particle packing dependent on the concentration c_s (as in the experiments of Mahgerefteh & Khodaverdian 1996). This constraining effect is then approximated by a rigid spherical shell of volume $(1/c_s)\pi d^3/6$ centred on the particle and surrounding its associated region of freely moving liquid. Assuming potential flow, the added mass associated with the motion of a spherical particle in such a shell is given by the exact expression (Lamb 1932, pp. 124-125)

$$\rho_a = \rho_w \frac{1 + 2c_s}{2(1 - c_s)}. \quad (39)$$

This expression reduces to the well-known result $\rho_a = \frac{1}{2}\rho_w$ in the dilute limit $c_s \rightarrow 0$. However as the concentration rises and the interstitial liquid is forced to flow within increasingly tight boundaries, much higher values of the added mass are attained. While the expression above involves no tuning parameter, it is obtained at the price of some drastic idealisations. Real liquid motions will involve vorticity and depend on the evolving

configuration of neighbouring particles. Endowed with their own trajectories, nearby particles will further respond to any sudden change (e.g due to a collision) in the motions of their neighbours (Sangani & Didwania 1993). Nevertheless, expression (39) can be hoped to provide a rough estimate of the added mass in fluctuating solid-liquid flows.

The influence of this added mass can then be incorporated into the stress functions in the way proposed by Kang *et al.* (1997) for dense bubble suspensions. The density ρ_s of the particle itself is supplemented by the added mass density ρ_a in the stress relations (35)-(36), i.e. we rewrite the normal and shear stress functions as

$$\sigma' = (1 + 4c_s g_0) c_s (\rho_s + \rho_a) T, \quad (40)$$

$$\tau = \frac{8c_s g_0 E}{5\pi^{1/2}} c_s (\rho_s + \rho_a) dT^{1/2} \dot{\gamma}, \quad (41)$$

where the dependence of the added mass on concentration $\rho_a(c_s)$ is given by (39). The resulting relations are plotted as dashed lines on Figures 26 and 27. For both the normal and shear stress functions, the added mass correction improves substantially the agreement of kinetic theory with the data.

4.5. Collision frequency

The collision frequency constitutes one further quantity for which the predictions of kinetic theory can be compared with the present data. A proxy for the collision frequency is furnished by the inverse correlation time of the fluctuation velocity. The correlation time is defined as the exponential decay time t_0 of the velocity autocovariance function. It is obtained in the

present experiments as a by-product of the procedure used to measure the granular temperature presented in Appendix 1. This exponential decay time t_0 can also be derived from the kinetic theory of dense gases (Chapman & Cowling 1970), leading to the following expression (Savage & Dai 1993):

$$\frac{1}{t_0} = \frac{8(1+e)}{\pi^{1/2}} c_s g_0 \frac{T^{1/2}}{d} \quad (42)$$

where e is the restitution coefficient ($e = 1$ for perfectly elastic particles) and $g_0(c_s)$ is again the function of concentration given by eq. (38). Expression (42) is similar to the theoretical collision frequency given by

$$\omega_{\text{coll}} = \frac{24}{\pi^{1/2}} c_s g_0(c_s) \frac{T^{1/2}}{d}. \quad (43)$$

The two expressions are not identical due to the fact that particles retain some memory of their previous velocity after a collision event (Chapman & Cowling 1970). For the case of elastic particles ($e = 1$), equations (42) and (43) indicate that the exponential decay time of the velocity autocorrelation is $3/2$ times longer than the mean time interval between collisions $\omega_{\text{coll}}^{-1}$. The correlation decay time t_0 is also related to the self-diffusion coefficient D through the relation

$$D = t_0 T \quad (44)$$

where T is the granular temperature. Studies of self-diffusion in dry granular flows have been conducted by Savage and Dai (1993), Campbell (1997), Hsiau and Shieh (1999), and Wildman *et al.* (1999).

Figure 28 compares the collision frequency function (43) with the measured autocorrelation

decay times t_0 derived from the observed particle trajectories (see Appendix 1). The normalised collision frequency $\omega_{\text{coll}}d/T^{1/2}$ is plotted against the solid concentration c_s , where the theoretical ω_{coll} is given by relation (43) and the measured ω_{coll} is approximated by

$$\omega_{\text{coll}} = \frac{3}{2}t_0^{-1} \quad (45)$$

i.e. the expression appropriate for perfectly elastic collisions. On Fig. 28, the collisional data from the different experimental runs are seen to collapse convincingly together. However the theoretical collision frequency (43) matches the inverse correlation time only for low solid concentrations c_s . For higher granular concentrations, the observed fluctuation velocities remain correlated longer (by up to one order of magnitude) than predicted. Thus agreement of theory and experiment for the collisional stresses does not guarantee that all features of collisional flow behaviour are well described by kinetic theory.

5. Conclusions

Using a recirculating flume and imaging techniques, the present work has sought to characterise in detail the vertical structure of steady uniform granular-liquid flows. For four different flow regimes (loose bed immature flow, mature flow and plug flow, and solid bed flow), depth profiles were obtained for the mean velocity, solid concentration, shear and normal stresses, and granular temperature. Based on these data, it was found possible to probe the local rheological behaviour of the flow as well as examine variations in behaviour over the flow depth. A rather painstaking inductive process was necessary to make sense of the experimental measurements, yet the overall picture which emerges is surprisingly coherent.

Gravity-driven granular-liquid flows are found to organise themselves into distinct sub-layers dominated by either frictional or collisional behaviour. Frictional behaviour is characterised

by 1) slow deformations; 2) a nearly constant ratio of mean shear rate to fluctuation velocity for which the Savage-Jeffrey parameter is close to unity ($R \approx 1$); 3) rate-independent shear and normal stresses which are proportional to each other. Collisional behaviour, on the other hand, is characterised by 1) rapid deformations; 2) a slightly variable ratio of mean shear rate to fluctuation velocity (from $R \approx 1$ up to $R \approx 2.5$); 3) quadratic dependence of the shear and normal stresses on the shear rate, with a variable ratio of shear to normal stress. From both a kinematic and kinetic point of view, therefore, the two behaviours exhibit distinct signatures.

The transition between frictional and collisional behaviour appears controlled by viscous effects. First, changes in the local flow rheology are observed to occur within a narrow range of the Stokes number, around $St = 5 \div 10$. Secondly, this Stokes number threshold also acts as a macroscopic constraint on the downslope flows: it defines the minimum value that must be attained by the maximum rate of shear of the slowest flows. Finally the same Stokes number range can be readily interpreted from a microscopic perspective: it corresponds to the threshold below which particles colliding in a viscous liquid cease to bounce off each other, as reported in various recent studies. Thus the available evidence conspires to suggest this surprising paradox: no viscous or macroviscous flow behaviour is observed alongside frictional and collisional behaviours, but the frictional-collisional transition seems controlled by viscosity.

Looking at the observed local rheology in greater detail, the present frictional measurements are found to be consistent with simple shear experiments conducted at the very low rates of shear typical of geotechnical tests. The collisional measurements, on the other hand, corroborate both the Bagnold description and the more recent kinetic theories of granular flows, even if the agreement requires some qualifications. In the present experiments, the shear and normal stresses do not exhibit a constant ratio, which runs counter to Bagnold's

description but agrees with Bagnold's own measurements. Overall, however, our results tend to confirm rather than undermine Bagnold's pioneering work. Turning to the kinetic theories, it was found possible to achieve quantitative agreement with the present measurements only by accounting for the inertia of the interstitial liquid. This is achieved by incorporating in the stress functions an added mass which varies with the solid concentration as if each particle moves about within a liquid-filled rigid shell.

To account for the present observations, it was not found necessary to invoke a hypothetical frictional-collisional regime which would blend at the microscale features associated with both frictional and collisional behaviours (as in the proposals of Johnson & Jackson 1987, or Savage 1998). Rather, our results suggest that the local behaviour is either frictional or collisional, and that the granular-liquid medium can switch between the two behaviours much like ice can melt into water. The behaviour shift would thus be analogous with a thermodynamic phase transition (as in the views proposed by Jenkins & Askari 1991, or Zhang & Campbell 1992). The gravity-driven flows observed in the present experiments appear rather sharply stratified into separate frictional and collisional sub-layers. Hence the term frictional-collisional regime would apply only in the macroscopic sense of flows exhibiting the two behaviours at different locations over their depth, without implying hybrid behaviour at the local level.

To be sure, the interpretation summarised above is open to argument and bound to be revised as experimental and theoretical work proceeds. Alternative interpretations of the present data are possible, and we have retained in the present paper only the explanations which we find most compelling. To compensate, we have tried to document the present experiments as completely as we could, and hope that this will allow the reader to come to his or her own conclusions.

The experiments and data are also subject to a number of significant limitations. Foremost among them is probably the two-dimensional nature of the sidewall measurements. The present 2D measurements are bound to reflect only partially the 3D conditions near the sidewall, and doomed to miss the 3D features of the flow inside the bulk. One specific limitation in this regard concerns the solid concentration measurements, for which the 2D pattern-based estimate breaks down in the dense limit. Because of this, the data gathered in the present work are not suited to examine the role of solid concentration in the frictional regime.

To address these limitations, efforts are under way to obtain three-dimensional measurements. Preliminary results in this direction are encouraging (see Larcher 2002; Spinewine *et al.* 2003). However the technical difficulties involved mean that the acquisition of a data set comparable in scope to the present one lies some distance into the future. Further improvements would also include direct measurements of stresses and pore pressures, to confirm and refine the force balance estimates used in the present work. Finally, experiments with liquids of different viscosities would be desirable to test the effect of viscosity on the flow behaviour in general and on the frictional-collisional transition in particular. New experimental efforts are definitely needed to further the understanding of granular-liquid flows.

This research benefited from the support of various people and institutions. The authors wish to extend special thanks to Luca Guarino (formerly at the University of Trento) for his contribution to the early stages of the work and for his encouragements of the later developments. Feed-back and assistance from S.B. Savage of McGill University, B.

Spinewine, J.-Fr. Vanden Berghe and Y. Zech of the UCLouvain, and D.-L. Young of the National Taiwan University are also gratefully acknowledged.

Financial support was provided by the Italian Group for Disaster Prevention (GNDCI) of the CNR, Italy, and by the European research projects THARMIT and IMPACT. Additional support for the participation of H. Capart was provided by the Fonds National de la Recherche Scientifique, Belgium, and the National Science Council, Taiwan, via grant no. 90-2211-E-002-084.

Appendix: Autocovariance-based estimation of the granular temperature

Velocity measurements obtained by particle-tracking velocimetry (PTV) are prone to errors due to limited spatial accuracy and finite sampling frequency. For the mean velocity components, these errors average out and can be made arbitrarily small provided a large ensemble of data is used. This is not the case, however, for the root-mean-square velocity fluctuations or, in the case of granular flows, the granular temperature. On the one hand, spurious contributions to the apparent fluctuation velocity arise due to measurement noise. On the other hand, attenuation of the apparent fluctuation velocity occurs due to the smoothing effect of finite sampling frequency. The present section outlines a procedure to correct for these effects when estimating the granular temperature from PTV measurements. The procedure is based on an examination of the Lagrangian velocity autocovariance functions.

Error model

To simplify the analysis, it is assumed that tracking mismatches have been previously filtered out. This is achieved in practice using the pattern and path-based methods detailed in Capart *et al.* (2002). Particle images observed on two successive frames can thus be unambiguously paired and associated to one and the same physical particle. We further assume that the particle is tracked over many successive frames, and restrict our attention to a single velocity component. The PTV estimate of the x -wise velocity history of the particle is given by (e.g. Adrian 1991)

$$\hat{u}^{(n)} = \frac{\hat{x}^{(n+1)} - \hat{x}^{(n)}}{t^{(n+1)} - t^{(n)}}, \quad (\text{A } 1)$$

where $\hat{x}^{(n)}$ is the measured position of the particle sampled at regularly spaced instants $t^{(n)} = n\Delta t$. To devise a simple error model, one can first assume that the measured position $\hat{x}^{(n)}$ is equal to the true particle position $x^{(n)} = x(t^{(n)})$ to which is added a random measurement error, i.e.

$$\hat{x}^{(n)} = x^{(n)} + s\epsilon^{(n)} \quad (\text{A } 2)$$

where s is the standard deviation of the measurement error on position, related to the pixel resolution of the images, and the $\epsilon^{(n)}$ are random variables of zero mean and unit standard deviation. We assume that successive position errors $\epsilon^{(n)}$ are uncorrelated, i.e.

$$\langle \epsilon^{(m)} \epsilon^{(n)} \rangle = 0 \quad m \neq n \quad (\text{A } 3)$$

where the brackets denote an average carried out over an ensemble of trajectories. Substituting (A2) into (A1) and invoking relation $x(t) = \int u(t)dt$, the following relationship is obtained between the measured velocity history $\hat{u}^{(n)}$ and the true velocity history $u(t)$ of a particle

$$\hat{u}^{(n)} = \tilde{u}^{(n)} + \frac{s}{\Delta t}(\epsilon^{(n+1)} - \epsilon^{(n)}), \quad (\text{A } 4)$$

where

$$\tilde{u}^{(n)} = \frac{1}{\Delta t} \int_{t^{(n)}}^{t^{(n+1)}} u(t) dt \quad (\text{A } 5)$$

represents the average of the unresolved particle velocity over time interval Δt . The above relationship constitutes an observation equation (Honerkamp 1998) for the PTV measurement process, i.e. an idealised description of the connection between the true signal and the observed one. Expression (A 4) accounts for two discrepancies between the measured velocity and the actual velocity. The first discrepancy is due to the discrete sampling of particle positions, which amounts to averaging the velocity over interval Δt and damps out high-frequency velocity fluctuations. The second discrepancy, expressed by the second term on the right hand side, is a corrupting noise due to random position error. One can immediately observe that

$$\langle \hat{u} \rangle = \langle \tilde{u} \rangle = \langle u \rangle = \bar{u} \quad (\text{A } 6)$$

i.e. neither the averaging nor the zero-mean noise on the position induce any bias on the average velocity. For the fluctuation components defined by

$$u'(t) = u(t) - \bar{u}, \quad \tilde{u}'^{(n)} = \tilde{u}^{(n)} - \bar{u}, \quad \hat{u}'^{(n)} = \hat{u}^{(n)} - \bar{u}, \quad (\text{A } 7)$$

however, the situation is not so favourable. Their mean squared values are not equivalent, i.e.

$$\langle \hat{u}'^2 \rangle \neq \langle \tilde{u}'^2 \rangle \neq \langle u'^2 \rangle. \quad (\text{A } 8)$$

Incidence on the velocity autocovariance function

Let us take a slightly more general view and examine the autocovariance functions (or acf in shorthand)

$$\langle u'(t)u'(t + \delta t) \rangle, \quad \langle \tilde{u}'^{(n)}\tilde{u}'^{(n+k)} \rangle, \quad \text{and} \quad \langle \hat{u}'^{(n)}\hat{u}'^{(n+k)} \rangle, \quad (\text{A } 9)$$

where δt is arbitrary but k is restricted to integer values. The averaged acf $\langle \tilde{u}'^{(n)}\tilde{u}'^{(n+k)} \rangle$ is related to the true acf $\langle u'(t)u'(t + \delta t) \rangle$ by the exact relation

$$\langle \tilde{u}'^{(n)}\tilde{u}'^{(n+k)} \rangle = 1/(\Delta t)^2 \left(\int_0^{\Delta t} dt' \int_0^{t'} dt'' \langle u'(t' + k\Delta t)u'(t'') \rangle + \int_0^{\Delta t} dt'' \int_0^{t''} dt' \langle u'(t' + k\Delta t)u'(t'') \rangle \right) \quad (\text{A } 10)$$

in which t' and t'' are variables of integration. Equation (A10) derives (after some developments) from definition (A5). It generalises a relation proposed by Batchelor (1949) and exploited by Hansen and McDonald (1986) and Campbell (1997) to analyse self-diffusion processes. The generalised relation (A10) and its usefulness in the context of PTV error analysis do not seem to have been reported before.

On the other hand, the measured acf $\langle \hat{u}'^{(n)}\hat{u}'^{(n+k)} \rangle$ (including the presence of noise) is related to the averaged acf $\langle \tilde{u}'^{(n)}\tilde{u}'^{(n+k)} \rangle$ by relation

$$\langle \hat{u}'^{(n)}\hat{u}'^{(n+k)} \rangle = \begin{cases} \langle \tilde{u}'^2 \rangle + \frac{2s^2}{(\Delta t)^2} & \text{if } k = 0, \\ \langle \tilde{u}'^{(n)}\tilde{u}'^{(n+1)} \rangle - \frac{s^2}{(\Delta t)^2} & \text{if } |k| = 1, \\ \langle \tilde{u}'^{(n)}\tilde{u}'^{(n+k)} \rangle & \text{if } |k| > 1. \end{cases} \quad (\text{A } 11)$$

which follows immediately from (A2) and the assumption that errors on successive particle positions are uncorrelated. An important consequence of this assumption is that the noise does not affect the acf beyond the first two points $k = 0$ and $k = 1$.

Signal model

To exploit the observations above, it is useful to adopt a simple model for the physical signal as well. Theoretical arguments by Hansen & McDonald (1986), computer simulations by Savage & Dai (1993) and by Campbell (1997) and experiments with vibro-fluidised disks by Wildman *et al.* (1999) indicate that for granular flows the short time behaviour of the physical velocity auto-correlation function should be well approximated by an exponential curve, i.e.

$$\langle u'(t)u'(t + \delta t) \rangle = \langle u'^2 \rangle \exp(-|\delta t|/t_0), \quad (\text{A } 12)$$

where the decay constant t_0 is related to the average time between successive particle collisions (Savage & Dai 1993). Substituting (A12) into (A10) and carrying out the integrations yields the explicit result

$$\frac{\langle \tilde{u}'^{(n)}\tilde{u}'^{(n+k)} \rangle}{\langle u'(t)u'(t+k\Delta t) \rangle} = \begin{cases} f(\Delta t/t_0) = 2\frac{t_0}{\Delta t} \left[1 + \frac{t_0}{\Delta t} \left[\exp\left(-\frac{\Delta t}{t_0}\right) - 1 \right] \right] & \text{if } k = 0, \\ g(\Delta t/t_0) = \frac{t_0^2}{(\Delta t)^2} \left[\exp\left(-\frac{\Delta t}{t_0}\right) + \exp\left(\frac{\Delta t}{t_0}\right) - 2 \right] & \text{if } |k| > 0, \end{cases} \quad (\text{A } 13)$$

The effect of finite sampling frequency on the signal is two-fold: first, the variance (corresponding to $k = 0$) is attenuated by a factor $f(\Delta t/t_0) < 1$; conversely, the tail of the autocovariance function ($|k| > 0$) is amplified by a factor $g(\Delta t/t_0) > 1$. As the function g is independent of k , furthermore, the tail of the observed acf retains an exponential shape governed by the same decay time t_0 as the physical acf. Under the assumptions of the simple model adopted above, it is therefore concluded that the tail of the observed autocovariance function $\langle \hat{u}'^{(n)}\hat{u}'^{(n+k)} \rangle$ ($k > 1$) is affected only in a very limited way by the two sources of

error which corrupt the variance $\langle \hat{u}'^2 \rangle$.

Corrected estimate of the granular temperature

The adopted correction procedure derives immediately from the observations above. Instead of choosing direct estimate $\langle \hat{u}'^2 \rangle$ for the mean square velocity fluctuations, the idea is to exploit the less corrupted information contained in the tail of the observed autocovariance function $\langle \hat{u}'^{(n)} \hat{u}'^{(n+k)} \rangle$ ($k > 1$). An exponential curve is fitted to this tail, keeping only the points $2 \leq k \leq m$, where m is a time cut-off chosen to avoid the deviations from exponential and the poorer statistics of the long-time tail. The fit yields an estimate for the decay time t_0 , as well as a revised zero-intercept $\langle u'^2 \rangle_{\text{fit}}$ for the acf. This latter estimate is affected by the amplification factor $g(\Delta t / t_0)$ given in (A13), which is easily accounted for by letting

$$\langle u'^2 \rangle_{\text{corr}} = \frac{\langle u'^2 \rangle_{\text{fit}}}{g(\Delta t / t_0)} \quad (\text{A } 14)$$

which is our corrected estimate for the mean square velocity fluctuations. Depending on whether the effect of noise or attenuation is prevalent, this value may be either lower or higher than the direct estimate $\langle \hat{u}'^2 \rangle$. In practice, we apply the above procedure jointly to the two components of the velocity vector $\mathbf{u} = (u, v)$ by considering the covariance $\langle \mathbf{u}'(t) \cdot \mathbf{u}'(t + \delta t) \rangle$. This allows us to derive a corrected estimate of the granular temperature

$$T = \frac{1}{2} \langle \mathbf{u}' \cdot \mathbf{u}' \rangle = \frac{1}{2} \langle u'^2 + v'^2 \rangle \quad (\text{A } 15)$$

and a single estimate of the correlation decay time t_0 .

As a further useful by-product, the procedure also yields an estimate for the rms error on particle position s . We get from (A13)

$$\langle \tilde{u}'^2 \rangle = f(\Delta t / t_0) \langle u'^2 \rangle_{\text{corr}}. \quad (\text{A } 16)$$

From (A11), on the other hand,

$$s = \frac{\Delta t}{\sqrt{2}} (\langle \hat{u}'^2 \rangle - \langle \tilde{u}'^2 \rangle)^{1/2} \quad (\text{A } 17)$$

which allows an *a posteriori* evaluation of the magnitude of the incurred position error.

Monte-Carlo tests

The theory and procedure presented above were checked using Monte-Carlo simulations. To synthesise an artificial ‘physical’ signal, a simple model derived from the Enskog theory of uncorrelated binary collisions is adopted (see Hansen and McDonald 1986). In this model, a single particle collides with other particles at random time intervals of mean duration t_0 . Particle velocities are constant between collisions, and each collision is assumed to completely decorrelate the velocity. Thus velocities on separate intervals are taken to be independent Gaussian variables of constant mean and standard deviation. For this process, the exponential velocity acf (A12) is exact with decay time equal to t_0 . Realisations of this process are straightforward to generate using typical Monte-Carlo methods (see e.g. Ross 1990). The ‘true’ random particle trajectories can be integrated exactly, and positions sampled at regular time intervals to simulate PTV measurements. Uncorrelated Gaussian noise of zero mean and constant standard deviation can then be added to the data to reproduce the random position errors.

‘True’ and observed fluctuation velocities $u'(t)$ and \hat{u}'_i generated in this fashion are plotted on panel (a) Fig. 29. The corresponding auto-covariance functions (acf) are shown on panel (b). Finally panel (c) compares raw rms values and corrected acf estimates with the true fluctuation velocity $T^{1/2}$, for various signal-to-noise ratios $T^{1/2}\Delta t/s$. The raw root-mean-square average $\langle \hat{u}'^2 \rangle^{1/2}$ (black dots) overestimates the fluctuation velocity when noise dominates, and underestimates the true value when attenuation dominates. In both cases,

the corrected estimate (A14) based on the Lagrangian acf (white squares) succeeds in recovering values closer to the true fluctuation velocity. All fluctuation velocity and granular temperature measurements reported in the present work were obtained using this procedure.

Sample results

Application of the autocovariance-based approach to actual measurements is illustrated on Fig. 30. Panel (a) shows actual acf results measured at mid-depth for experimental run 85. Overall, the observed shape of the autocovariance function is consistent with the assumptions of the present analysis. There is however one significant difference: errors on particle position include a periodic perturbation at a frequency of 50 Hz in addition to uncorrelated random noise. This shows up on the autocovariance plot of panel (b) as high-frequency saw teeth. By filming a bed of particles at rest under conditions identical to those of the experiments, it was checked that this noise is due to a faint flickering of the halogen lamps used to illuminate the flows. Since this noise occurs at sufficiently high frequency, however, it does not affect the low frequency acf fit used to estimate the granular temperature. Using relation (A17) the root-mean-squared error on particle position was estimated to be of the order of 0.2 pixel in the present experiments. This is comparable to the error magnitude reported by Veber *et al.* (1997) in their analysis of PTV accuracy.

Panel (b) of Fig. 30 shows the fluctuation velocity profile $T^{1/2}$ of run 85. The values of fluctuation velocity $T^{1/2}$ obtained using the direct rms estimate and those obtained using the acf-based correction procedure are plotted as solid and dashed curves, respectively. The correction procedure is applied separately to each of the 20 averaging bins shown earlier on Fig. 7. The noise component is seen to be the predominant source of error, causing the direct root-mean-squared average to overestimate the fluctuation velocity. In relative terms, this effect is most severe in the lowermost part of the flow, where the granular motion is slow.

Below a depth $y \approx 9$ cm, the grains are actually motionless, as indicated by the mean velocity profile of the same run plotted on Fig. 7. The direct estimate nonetheless yields a finite value of the fluctuation velocity. By contrast, the corrected estimate successfully filters out the noise component. Error bars on Fig. 30b represent the statistical error (± 2 standard deviations) associated with the estimates. This statistical error is evaluated by coarse-graining (see e.g. Rapaport 1995): quantities are estimated on 10 separate data subsets rather than the full data set, then the standard deviation of the 10 resulting numbers is divided by $\sqrt{10}$ to approximate the standard deviation of their average. Due to the large data set acquired in the present experiments, the statistical errors are small. In this case they are also rather poor indicators of the actual measurement errors. The small error bars around the raw rms values at the bottom of the flow, for instance, indicate only that noise is measured very precisely, not that the signal is accurately captured ! For this reason, a better indication of the uncertainty associated with the present measurements is probably provided by the data scatter between different experimental runs.

References

- Adrian, R.J. 1991. Particle-imaging techniques for experimental fluid mechanics. *Annu. Rev. Fluid Mech.* **23**, 261-304.
- Aharonov, E., & Sparks, D. 1999. Rigidity phase transition in granular packings. *Phys. Rev. E* **60**(6), 6890-6896.
- Ahn, H., Brennen, C.E., & Sabersky, R.H. 1991. Measurements of velocity, velocity fluctuation, density, and stresses in chute flows of granular materials. *Trans. ASME E: J. Appl. Mech.* **58**(3), 792-803.
- Allen, M.P. & Tildesley, D.J. 1987. *Computer Simulations of Liquids*. Clarendon.
- Ancey, C. 2002. Dry granular flows down an inclined channel: Experimental investigations on the frictional-collisional regime. *Phys. Rev. E* **65**(1), art. no. 011304.
- Aragon, J.A.G. 1995. Granular-fluid chute flow – experimental and numerical observations. *J. Hydr. Engrg* **121**(4), 355-364.
- Armanini, A., Fraccarollo, L., Guarino, L., Martino, R., & Bin, Y. 2000. Experimental analysis of the general features of uniform debris flow over a loose bed. In Wieczorek, G.F. & Naeser, N.D. (eds) *Proc. 2nd Int. Conf. on Debris-Flow Hazards Mitigation*, Taipei, Taiwan (August 2000), pp. 327-334. Balkema.
- Asano, T. 1995. Sediment transport under sheet-flow conditions. *J. Waterw. Port Coast. Oc. Engrg* **121**(5), 239-246.
- Azanza, E., Chevoir, F., & Moucheront, P. 1999. Experimental study of collisional granular flows down an inclined plane. *J. Fluid Mech.* **400**, 199-227.
- Bagnold, R.A. 1954. Experiments on a gravity-free dispersion of large solid spheres in a Newtonian fluid under shear. *Proc. Roy. Soc. London A* **225**, 49-63.
- Bakthiary, A.Y., & Asano, T. 1998. Effects of particle properties on oscillatory sheet-flow dynamics. *JSCE Coastal Engrg J.* **40**(1), 61-80.
- Batchelor, G.K. 1949. Diffusion in a field of homogeneous turbulence: I. Eulerian analysis. *Austral. J. Sci. Res.* **2**, 437-450.
- Batchelor, G.K. 1988. A new theory of the instability of a uniform fluidized bed. *J. Fluid Mech.* **193**, 75-110.
- Bauer, E. 1996. Calibration of a comprehensive hypoplastic model for granular materials. *Soils and Foundations* **36**, 13-26.

- Campbell, C.S. 1989. The stress tensor for simple shear flows of a granular material. *J. Fluid Mech.* **203**, 449-473.
- Campbell, C.S. 1990. Rapid granular flows. *Annu. Rev. Fluid Mech.* **22**, 57-92.
- Campbell, C.S. 1997. Self-diffusion in granular shear flows. *J. Fluid Mech.* **348**, 85-101.
- Campbell, C.S., & Brennen, C.E. 1985. Computer simulations of granular shear flows. *J. Fluid Mech.* **151**, 167-188.
- Capart, H., Fraccarollo, L., Guarino, L., Armanini, A. & Zech, Y. 2000. Granular temperature behaviour of loose bed debris flows. In Wieczorek, G.F. & Naeser, N.D. (eds) *Proc. 2nd Int. Conf. on Debris-Flow Hazards Mitigation*, Taipei, Taiwan (August 2000), pp. 361-368. Balkema.
- Capart, H., Young, D.L. & Zech, Y. 2002. Voronoï imaging methods for the measurement of granular flows. *Exp. Fluids* **32**, 121-135.
- Carnahan, N.F., & Starling, K.E. 1969. Equation of state for nonattracting rigid spheres. *J. Chem. Phys.* **51**(2), 635-636.
- Castro, G. & Poulos, S.J. 1977. Factors affecting liquefaction and cyclic mobility. *ASCE J. Geotech. Engng Div.* **106**, 501-506.
- Chang, H.C., Demekhin, E.A. & Kalaidin, E. 2000. Coherent structures, self-similarity, and universal roll wave coarsening dynamics. *Phys. Fluids* **12**, 2268-2278.
- Chapman, S., & Cowling, T.G. 1971. *The mathematical theory of non-uniform gases*. Third edition, Cambridge Univ. Press.
- Courrech du Pont, S., Gondret, P., Perrin, B., & Rabaud, M. 2003. Granular avalanches in fluids. *Phys. Rev. Lett.* **90**(4): art. no. 044301.
- Das, B.M. 1990. *Principles of Geotechnical Engineering*. PWS-KENT.
- Davies, T.R.H. 1988. Debris Flow Surges – A Laboratory Investigation. *Mitteilungen der Versuchsanstalt für Wasserbau, Hydrologie und Glaziologie* Nr. 96, Technischen Hochschule Zürich.
- Davis, R.H., Serayssol, J.M., & Hinch, E.J. 1986. The elastohydrodynamic collision of two spheres. *J. Fluid Mech.* **163**, 479-497.
- Drake, T.G. 1991. Granular flow: physical experiments and their applications for microstructural theories. *J. Fluid Mech.* **225**, 121-152.
- Drake, T.G. & Calantoni, J. 2001. Discrete particle model for sheet flow sediment transport in

- the neashore. *J. Geophys. Res.* **106**(C9), 19859-19868.
- Dyvik, R., Berre, T., Lacasse, S. & Raadim, B. 1987. Comparison of truly undrained and constant volume direct simple shear tests. *Géotechnique* **37**, 3-10.
- Egashira, S., Itoh, T., & Takeuchi, H. 2001. Transition mechanism of debris flows over rigid bed to over erodible bed. *Phys. Chem. Earth B* **26**(2), 169-174.
- Elliott, K.E., Ahmadi, G., & Kvasnak, W. 1998. Couette flow of a granular mono-layer – an experimental study. *J. Non-Newtonian Fluid Mech.* **74**, 89-111.
- Goldhirsch, I. 2003. Rapid granular flows. *Annu. Rev. Fluid Mech.* **35**, 267-293.
- Gondret, P., Lance, M., & Petit, L. 2002. Bouncing motion of spherical particles in fluids. *Phys. Fluids* **14**(2), 643-652.
- Guarino, L. 1998. *Moto uniforme a superficie libra di misture granulari solido-liquido ad alta concentrazione*. B. Eng. Thesis, Università degli studi di Trento, Italy.
- Guler, M., Edil, T.B. & Bosscher P.J. 1999. Measurement of particle movement in granular soils using image analysis. *J. Comp. Civ. Eng.* **13**(2), 116-122.
- Hanes, D.M., & Inman, D.L. 1985. Observations of rapidly flowing granular-fluid mixtures. *J. Fluid Mech.* **150**, 357-380.
- Hansen, J.-P., & McDonald, I.R. 1986. *Theory of Simple Liquids*. Second edition, Academic Press.
- Hill, H.M. 1966. Bed forms due to a fluid stream. *ASCE J. Hydr. Div.* **92**, 127-143.
- Honerkamp, J. 1998. *Statistical Physics*. Springer.
- Hsiau, S.S. & Jang, H.W. 1998. Measurements of velocity fluctuations of granular materials in a shear cell. *Exp. Therm. Fluid Sci.* **17**, 202-209.
- Hsiau, S.S. & Shieh, Y.M. 1999. Fluctuations and self-diffusion of sheared granular material flows. *J. Rheol.* **43**, 1049-1066.
- Hsu, T.-J., Jenkins, J.T., & Liu, P.L.-F. 2004. On two-phase sediment transport: sheet flow of massive particles. *Proc. Roy. Soc. London A* **460**, 2223-2250.
- Huang, H.T., Fiedler, H.E. & Wang, J.J. 1993. Limitation and improvement of PIV. Part I: Limitation of conventional techniques due to deformation of particle image patterns. *Exp. Fluids* **15**, 168-174.
- Hunt, M.L., Zenit, R., Campbell, C.S., & Brennen, C.E. 2002. Revisiting the 1954 suspension experiments of R.A. Bagnold. *J. Fluid Mech.* **452**, 1-24.

- Iverson, R.M. 1997. The physics of debris flows. *Reviews of Geophysics* **35**, 245-296.
- Jaeger, H.M., Nagel, S.R., & Behringer, R.P. 1996. Granular solids, liquids, and gases. *Reviews of Modern Physics* **68**, 1259-1273.
- Jähne, B. 1995. *Digital Image Processing*. Springer.
- Jenkins, J.T., & Askari, E. 1991. Boundary conditions for rapid granular flows: phase interfaces. *J. Fluid Mech.* **223**, 497-508.
- Jenkins, J.T., & Hanes, D.M. 1998. Collisional sheet-flow of sediment driven by a turbulent fluid. *J. Fluid Mech.* **370**, 29-52.
- Jenkins, J.T., & Savage, S.B. 1983. A theory for the rapid flow of identical, smooth, nearly elastic particles. *J. Fluid Mech.* **130**, 186-202.
- Johnson, P.C., & Jackson, R. 1987. Frictional-collisional constitutive relations for granular materials, with application to plane shearing. *J. Fluid Mech.* **176**, 67-93.
- Joseph, G.G., Zenit, R., Hunt, M.L., & Rosenwinkel, A.M. 2001. Particle-wall collisions in a viscous fluid. *J. Fluid. Mech.* **433**, 329-346.
- Kalthoff, W., Schwarzer, S., & Herrmann, H. 1997. An algorithm for the simulation of particulate suspensions with inertia effects. *Phys. Rev. E* **56**(2), 2234-2242.
- Kang, S.-Y., Sangani, A.S., Tsao, H.-K., & Koch, D.L. 1997. Rheology of dense bubble suspensions. *Phys. Fluids* **9**(6), 1540-1561.
- Koch, D.L., & Hill, R.J. 2001. Inertial effects in suspension and porous-media flows. *Annu. Rev. Fluid Mech.* **33**, 619-647.
- Lamb, H. 1932. *Hydrodynamics*. Sixth edition. Cambridge Univ. Press.
- Larcher, M. 2002. *Vertical structure of high-concentration liquid-granular flows*. PhD thesis, joint programme of the Università degli Studi di Padova and Università degli Studi di Trento, Italy.
- Liggett, J.A. 1994. *Fluid Mechanics*. McGraw-Hill.
- Louge, M.Y. 2003. Model for dense granular flows down bumpy inclines. *Phys. Rev. E* **67**, 061303, 1-11.
- Louge, M.Y. & Jenkins J.T. 1997. Microgravity segregation in binary mixtures of inelastic spheres driven by velocity fluctuation gradients. In Chang, C.S., Misra, A., Liang, , R.Y. & Babic, M. (eds) *Mechanics of deformation and flow of particulate materials*, pp. 370-379. ASCE.

- Louge, M.Y. & Keast, S.C. 2001. On dense granular flows down flat frictional inclines. *Phys. Fluids* **13**, 1213-1233.
- Lun, C.K.K., Savage, S.B., Jeffrey, D.J., & Chepurniy, N. 1984. *J. Fluid Mech.* **140**, 223-256.
- Mahgerefteh, H., & Khodaverdian, A. 1996. Added mass effects in two-phase solid/liquid media. *Trans. Inst. Chem. Eng.* **74 A**, 272-280.
- Major, J.J., & Iverson, R.M. 1999. Debris-flow deposition – Effects of pore-fluid pressure and friction concentrated at flow margins. *Geol. Soc. Amer. Bull.* **111**, 1424-1434.
- Natarajan, V.V.R., Hunt, M.L., & Taylor, E.D. 1995. Local measurements of velocity fluctuations and diffusion coefficients for a granular material flow. *J. Fluid Mech.* **304**, 1-25.
- Ogawa, S. 1978. Multitemperature theory of granular materials. In *Proc. U.S.-Japan Seminar on Continuum-Mechanical and Statistical Approaches in the Mechanics of Granular Materials*. Tokyo: Gukujutsu Bunken Fukyukai, pp. 208-217.
- Okabe, A., Boots, B. & Sugihara, K. 1992. *Spatial Tessellations: Concepts and Applications of Voronoï Diagrams*. Wiley.
- Pan, T.W., Joseph, D.D., Bai, R., Glowinski, R., & Sarin, V. 2002. Fluidization of 1024 spheres: simulation and experiment. *J. Fluid. Mech.* **451**, 169-191.
- Parker, G. 2000. *Lecture notes, Summer School on Geomorphological Fluid Mechanics*, St. Oyen, Italy, June 2000.
- Prasad, S.N., Pal, D. & Romkens, M.J.M. 2000. Wave formation on a shallow layer of flowing grains. *J. Fluid. Mech.* **413**, 89-110.
- Rapaport, D.C. 1995. *The Art of Molecular Dynamics Simulation*. Cambridge University Press.
- Russo, G., & Smereka, P. 1996. Kinetic theory for bubbly flow II: fluid dynamic limit. *SIAM J. Appl. Math.* **56**(2), 358-371.
- Sangani, A.S., & Didwania, A.K. 1993. Dynamic simulations of flows of bubbly liquids at large Reynolds numbers. *J. Fluid Mech.* **250**, 307-337.
- Sangani, A.S., Mo, G., Tsao, H.-K., & Koch, D.L. 1996. Simple shear flows of dense gas-solid suspensions at finite Stokes numbers. *J. Fluid Mech.* **313**, 309-341.
- Savage, S.B. 1998. Analyses of slow high-concentration flows of granular materials. *J. Fluid Mech.* **377**, 1-26.

- Savage, S.B., & Dai, R. 1993. Studies of granular shear flows. Wall slip velocities, 'layering' and self-diffusion. *Mech. Mater.* **16**, 225-238.
- Savage, S.B., & Jeffrey, D.J. 1981. The stress tensor in a granular flow at high shear rates. *J. Fluid Mech.* **110**, 255-272.
- Savage, S.B., & McKeown, S. 1983. Shear stresses developed during rapid shear of concentrated suspensions of large spherical particles between concentric cylinders. *J. Fluid Mech.* **127**, 453-472.
- Sethi, I.K., & Jain R. 1987. Finding trajectories of feature points in a monocular image sequence. *IEEE Trans. Pattern Anal. Machine Intell.* **9**, 56-73.
- Shook, C.A., Gillies, R., Haas, D.B., Husband, W.H.W. & Small, M. 1982. Flow of coarse and fine sand slurries in pipelines. *J. Pipelines* **3**, 13-21.
- Silbert L.E., Ertas, D., Grest, G.S., Halsey, T.C., Levine, D., & Plimpton, S.J. 2001. Granular flow down an inclined plane: Bagnold scaling and rheology. *Phys. Rev. E* **64**, 051302.
- Spence, K.J., & Guymer I. 1997. Small-scale laboratory flowslides. *Géotechnique* **47**, 915-932.
- Spinewine, B., Capart, H., Larcher, M., & Zech, Y. 2003. Three-dimensional Voronoï imaging methods for the measurement of near-wall particulate flows. *Exp. Fluids* **34**, 227-241.
- Sumer, B.M., Kozakiewicz, A., Fredsøe, J., & Deigaard, R. 1996. Velocity and concentration profiles in sheet-flow layer of movable bed. *J. Hydr. Engrg.* **122**(10), 549-558.
- Taberlet, N., Richard, P., Valance, A., Losert, W., Pasini, J.M., Jenkins, J.T., & Delannay, R. Superstable Granular Heap in a Thin Channel. *Phys. Rev. Lett.* **91**(26), 264301, 1-4.
- Takahashi, T. 1991. *Debris Flow*. IAHR Monograph. Rotterdam: Balkema.
- Tubino, M., & Lanzoni, S. 1993. Rheology of debris flows: experimental observations and modelling problems. *Excerpta* **7**, 201-235.
- Vanden Berghe, J.-F., Holeymen, A. & Dyvik, R. 2001. Comparison and modeling of sand behavior under cyclic direct simple shear and cyclic triaxial testing. In Prakash S. (ed.) *Proc. 4th Int. Conf. on Recent Advances in Geotechnical Earthquake Engineering and Soil Dynamics*, San Diego (CD ROM).
- Veber, P., Dahl, J., & Hermansson, R. 1997. Study of the phenomena affecting the accuracy of a video-based Particle Tracking Velocimetry technique. *Exp. Fluids* **22**, 482-488.
- Wildman, R.D., Huntley, J.M., & Hansen, J.-P. 1999. Self-diffusion of grains in a two-dimensional vibrofluidized bed. *Phys. Rev. E* **60**(6), 7066-7075.

- Yeganeh, A., Gotoh, H., & Sakai, T. 2000. Applicability of Euler-Lagrange coupling multiphase-flow model to bed-load transport under high bottom shear. *J. Hydr. Res.* **38**(5), 389-398.
- Zenit, R., Hunt, M.L., & Brennen, C.E. 1997. Collisional particle pressure measurements in solid-liquid flows. *J. Fluid. Mech.* **353**, 261-283.
- Zenit, R., Hunt, M.L., & Brennen, C.E. 1998. On the direct and radiated components of the collisional particle pressure in liquid-solid flows. *Appl. Sci. Res.* **58**, 305-317.
- Zhang, D.Z., & Rauenzahn, R.M. 1997. A viscoelastic model for dense granular flows. *J. Rheol.* **41**(6), 1275-1298.
- Zhang, Y., & Campbell, C.S. 1992. The interface between fluid-like and solid-like behavior in two-dimensional granular flows. *J. Fluid Mech.* **237**, 541-568.
- Zuber, N. 1964. On the dispersed two-phase flow in the laminar flow regime. *Chem. Eng. Sci.* **19**, 897.

Tables

Table 1: Properties of the cylindrical PVC pellets used as granular material in the experiments

Parameter	Value	Test method	Comments
Density ρ_s [g/cm ³]	1.54	Pycnometer	Average of 3 tests
Particle height [mm]	2.8	Calypter	
Particle base diameter [mm]	3.2	Calypter	
Equivalent spherical diameter d [mm]	3.7	Diameter of a sphere of identical volume	From the measured volume of 500 pellets
Maximum concentration $c_s^{(\max)}$ [-]	0.69	Compaction	
Static friction angle [degrees]	35	Tilting board	At loose poured concentration $c_s \approx 0.6$.
Critical friction angle θ_c [degrees]	31	Simple shear test	Ratio of shear to effective normal stress at steady flow state (see Fig. 3)
Coefficient of permeability k [m/s]	$k = 0.098 \times e^3 / (1 + e) + 0.024$ obtained by fitting Kozeny-Carmen equation (Das 1990; Spence & Guymer 1997) through the data of Fig. 4	Permeameter / fluidisation cell	Data measured using a permeameter for static assemblies at concentration $c_s = 0.58$ and 0.65 , and using a fluidisation cell for the range of concentration $c_s = 0.4-0.5$
Specific retention S_r [-]	0.08	Comparison of wet and dry weights of bulk sample	Volume fraction of water retained due to surface tension upon gravity drainage of a saturated sample
Height of capillary rise h_c [mm]	in the interval between 5 and 15 mm	Tulip test	Difference in height between the top of a saturated sample and the water level of a connected reservoir at which the sample desaturates

Table 2: Parameters of the experimental runs selected for detailed imaging analysis

Flow regime	Run no.	Plot Symbols ¹	Slope β [deg]	Total discharge $Q^{(\text{bulk})}$ [l/s]	Transport concentration C_s	Flow thickness H [cm]	Mean velocity U [m/s]
Immature, sheet-flow	11	△ ▲	6.9	5.81	0.430	3.2	0.47
	83	▷ ►	7.4	9.15	0.465	5.3	0.69
	84	▽ ▼	6.2	4.21	0.346	2.5	0.60
	85	◀ ◆	6.2	4.71	0.346	2.2	0.60
Mature flow	5	□ ▾	8.4	10.33	0.529	7.1	0.48
	88	▽ ▷	8.1	5.75	0.504	5.2	0.33
	90	▽ ▾	8.5	7.50	0.511	6.6	0.40
	91	△ ▲	8.4	6.73	0.508	7.0	0.41
Partially unsaturated plug flow	6	□ ◁	12	5.34	0.525	8.0	0.21
	104	□ ▲	10.7	9.64	0.503	12.6	0.28
	105	▷ ▷	12.3	9.93	0.511	12.9	0.27
	106	□ ▾	12.4	10.98	0.515	12.6	0.29
Solid bed flow	38	□ ■	19	12.57	0.514	3.0	1.36
	41	◇ ♦	22	10.04	0.542	3.1	1.35
	42	◇ ♦	22	10.13	0.516	2.7	1.48
	46	○ ●	23	12.43	0.493	2.7	1.65

¹ Hollow symbols denote collisional behaviour, and filled symbols denote frictional behaviour, as determined on the basis of the local Stokes number St' (see explanations in section 4.3).

Figure captions

Figure 1. Multiple exposure image of a granular-liquid flow over loose bed, showing the rapidly flowing layer and underlying static deposit (run 85 from the present experiments).

Figure 2. Trento recirculating flume developed for the study of steady uniform debris flows:
(a) side view; (b) downstream view; (c) plane view.

Figure 3. Results of the simple shear tests. Solid lines: measured stress paths for four different tests, each characterised by distinct void ratios e at the beginning and end of the test; dashed line: steady state locus.

Figure 4. Variation of permeability as a function of void ratio e . Crosses (+): data from the permeameter and fluidisation cell tests; solid line: Kozeny-Carmen fit.

Figure 5. Pattern-based particle tracking algorithm (Capart *et al.* 2002): (a) image detail with positioned particle centres; (b) Voronoï diagram constructed on the sets of particle centres identified on one frame (thin lines) and the next (thick lines); (c) displacement vectors obtained by pairing nearby particles having similar Voronoï cells.

Figure 6. Velocimetry results: (a) sample image frame (from sheet-flow run 85); (b) displacement vectors obtained by tracking grains on two successive frames (grain positions for which no matches were found are circled on the plot); (c) granular trajectories derived from 100 successive image frames; (d) convected trajectories obtained by subtracting the mean flow component from particle tracks extracted from 50 successive frames.

Figure 7. Averaging of raw velocity data (from sheet-flow run 85): (a) cloud of circa 170,000 velocity data points obtained by tracking particles over 500 frames (black symbols: longitudinal velocity; gray symbols: vertical velocity; lines: bin limits); (b) mean velocities averaged over separate sub-intervals to check steady uniform character of the flow; (c) velocity profiles averaged from full sequence (solid lines: mean velocities;

dashed lines: root-mean-squared fluctuation velocity plotted on both sides of the corresponding means).

Figure 8. Relationship between the channel inclination β and the Froude number Fr for uniform granular-liquid flows: (+) solid bed, transport concentration $C_s^{(\text{bulk})} = 0.51 - 0.53$; (+) solid bed, transport concentration $C_s^{(\text{bulk})} = 0.53 - 0.55$; (\times) loose bed. Solid bed data are derived from direct depth and discharge measurements, and loose bed data from depth-integrated imaging estimates.

Figure 9. Relationship between channel inclination β and transport concentration C_s for uniform loose bed flows. Crosses (\times): transport concentration data (bulk measurements $C_s^{(\text{bulk})}$ obtained at the channel outlet) for a set of 40 experimental runs; Solid line: equation (23) based on macroscopic force balance.

Figure 10. Typology of the examined flows: (a) loose bed, immature flow (sheet-flow); (b) loose bed, mature flow; (c) loose bed, plug flow; (d) solid bed flow.

Figure 11. Kinetic energy time history used as a check of the steady character of the observed flows: (a) solid bed runs 41 and 46. (b) loose bed runs 85, 90, and 105.

Figure 12. Particularly strong roll waves observed in solid bed run 46: phase trajectory on a plot of potential versus kinetic energy.

Figure 13. Velocity distribution over the channel cross-section: (a) surface velocity across the channel width (run 41); (b) velocity depth profile at the sidewall (run 41); (c) hypothetical 3D velocity distribution for a typical loose bed run.

Figure 14. Depth-integrated estimates based on sidewall imaging measurements compared with bulk measurements at the outlet: (a) total discharge $Q^{(\text{imag})}$ vs. $Q^{(\text{bulk})}$; (b) transport granular concentration $C_s^{(\text{imag})}$ vs. $C_s^{(\text{bulk})}$.

Figure 15. Depth profiles for the sheet-flow regime: (a) mean velocity; (b) solid concentration (gray band indicates range in which concentration measurements are uncertain); (c) shear

rate; (d) fluctuation velocity. See Table 2 for symbol legends.

Figure 16. Depth profiles for the mature flow regime: (a) mean velocity; (b) solid concentration; (c) shear rate; (d) fluctuation velocity.

Figure 17. Depth profiles for the plug flow regime: (a) mean velocity; (b) solid concentration; (c) shear rate; (d) fluctuation velocity.

Figure 18. Depth profiles for the solid bed flows: (a) mean velocity; (b) solid concentration; (c) shear rate; (d) fluctuation velocity.

Figure 19. Variation of the normalised shear stress $\tau / [\mu_w^2 \lambda / (\rho_s d^2)]$ with the local Bagnold number $Ba = (\rho_s \lambda^{1/2} d^2 / \mu_w) \dot{\gamma}$. See Table 2 for symbol legends. The relationships proposed by Bagnold (1954) for the macro-viscous and grain-inertia regimes are shown as dashed and solid lines, respectively.

Figure 20. Variation of the normalised effective normal stress $\sigma' / [\mu_w^2 \lambda / (\rho_s d^2)]$ with the local Bagnold number $Ba = (\rho_s \lambda^{1/2} d^2 / \mu_w) \dot{\gamma}$. The relationships proposed by Bagnold (1954) for the macro-viscous and grain-inertia regimes are shown as dashed and solid lines, respectively.

Figure 21. Variation of the stress ratio τ / σ' with the local Bagnold number $Ba = (\rho_s \lambda^{1/2} d^2 / \mu_w) \dot{\gamma}$. The constant values proposed by Bagnold (1954) for the macro-viscous and grain-inertia regimes are shown as dashed lines, while the solid line represents the stress ratio measured with the simple shear apparatus (Table 1).

Figure 22. Relationship between shear rate $\dot{\gamma}$ and fluctuation velocity $T^{1/2}$, made dimensionless using Stokes numbers $St = \frac{1}{18}(\rho_s / \rho_w)d^2\dot{\gamma} / \nu_w$ and $St' = \frac{1}{18}(\rho_s / \rho_w)dT^{1/2} / \nu_w$.

Figure 23. Macroscopic behaviour of steady uniform granular-liquid flows over loose beds: dependence of the normalised maximum shear rate $St_{\max} = \frac{1}{18}(\rho_s / \rho_w)d^2\dot{\gamma}_{\max} / \nu_w$ on flow inclination β .

Figure 24. Comparison of the present collisional data ($St > St^*$) with Bagnold's normal stress function. Gray band indicates range in which concentration measurements are uncertain.

Figure 25. Comparison of the present collisional data ($St > St^*$) with Bagnold's shear stress function.

Figure 26. Comparison of the present collisional data ($St > St^*$) with the normal stress function of kinetic theory. Solid line: basic theory (Jenkins & Hanes 1998); dashed line: revised theory with added mass correction.

Figure 27. Comparison of the present collisional data ($St > St^*$) with the shear stress function of kinetic theory. Solid line: basic theory (Jenkins & Hanes 1998); dashed line: revised theory with added mass correction.

Figure 28. Comparison of measured inverse correlation time with the collision frequency predicted by kinetic theory.

Figure 29. Monte-Carlo simulations of PTV measurements: (a) fluctuation velocity histories (solid line: ‘true’ signal $u'(t)$, dots: PTV data \hat{u}'_i); (b) velocity autocovariance functions (dashed line: true acf, solid line: attenuated acf, dots: measured acf); (c) measured fluctuation velocity against true value for various signal-to-noise ratios (black dots: direct estimate, white squares: corrected estimate, diagonal: line of perfect agreement).

Figure 30. Estimation of fluctuation velocities based on the Lagrangian autocovariance function (acf): (a) acf measured at mid-depth for run 85 (dots: measured acf; dashed line: exponential fit); (b) comparison of direct (solid line/black dots) and corrected estimates (dashed line/white squares) of the fluctuation velocity profile for run 85. Error bars indicate ± 2 standard deviations estimated by coarse-graining.

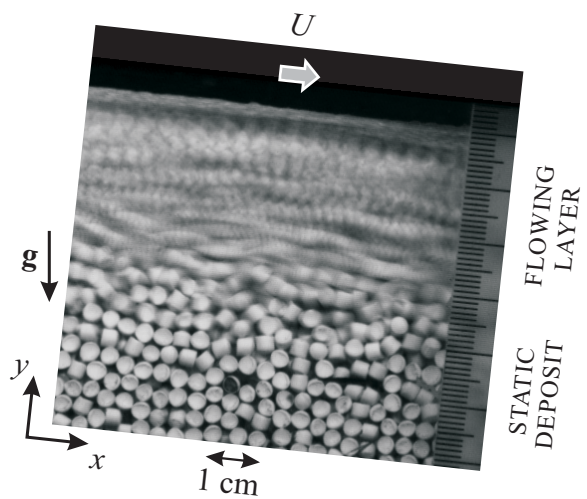


Figure 1

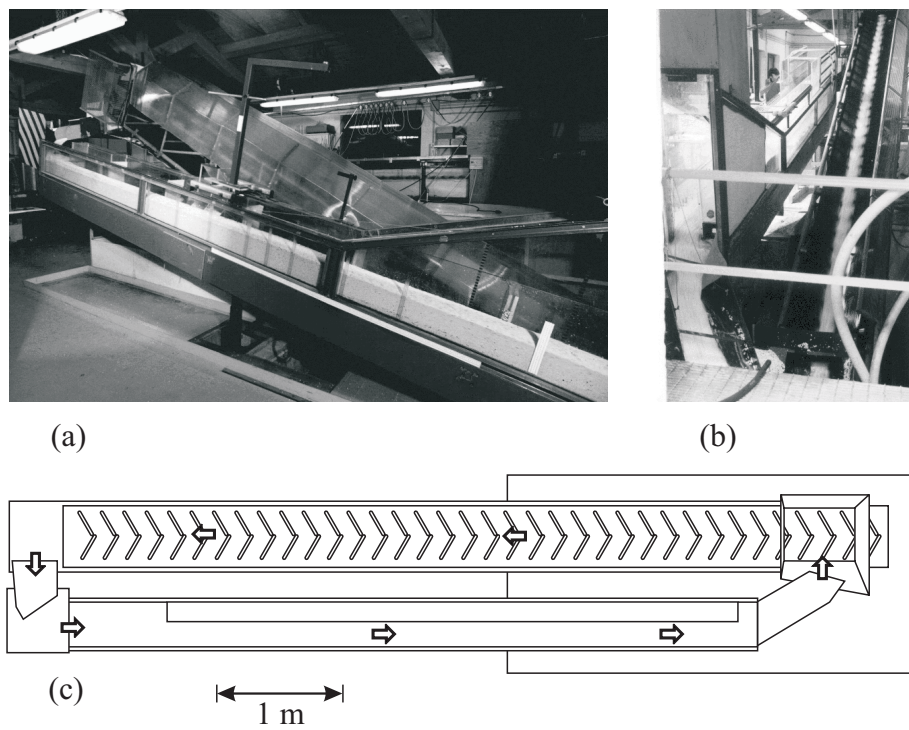


Figure 2

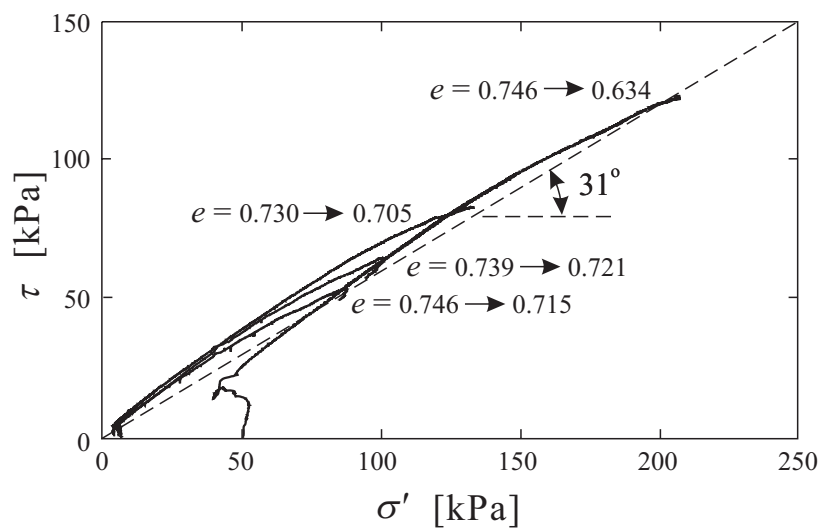


Figure 3

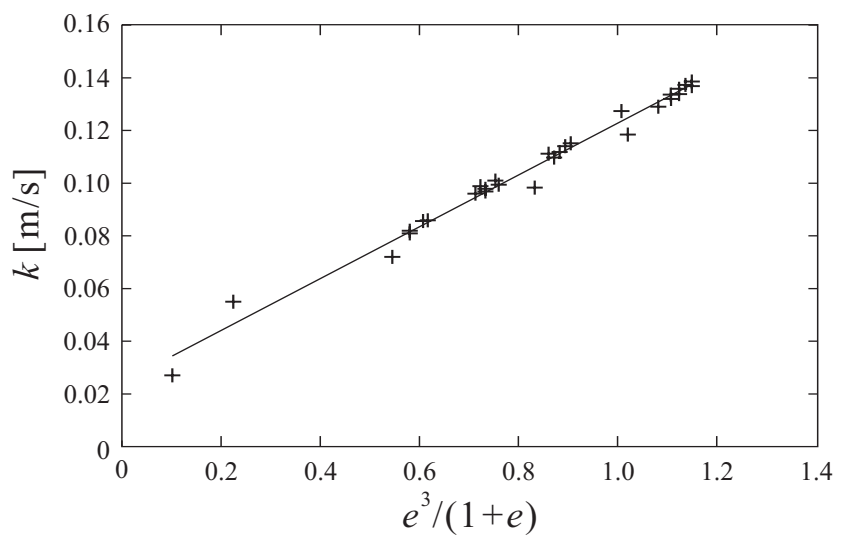


Figure 4

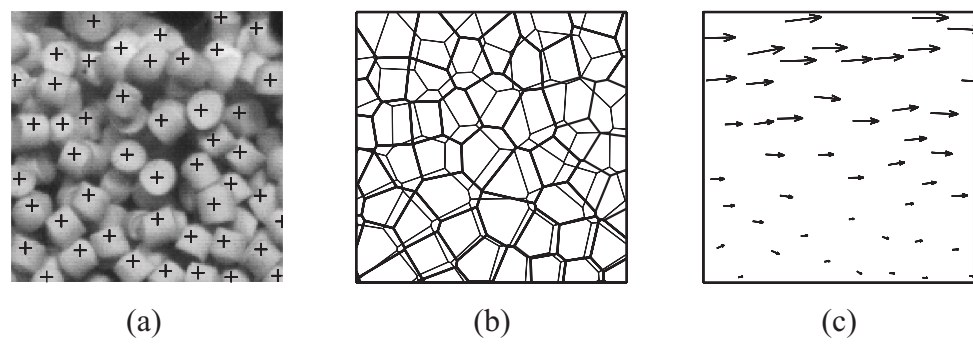


Figure 5

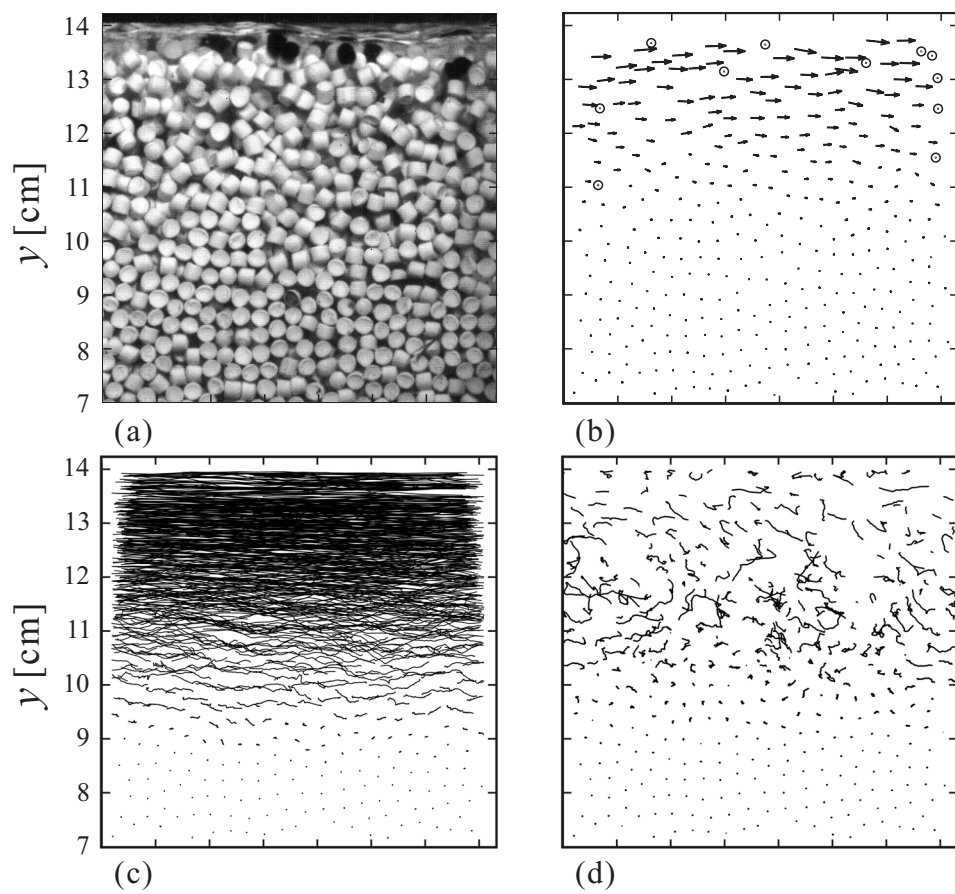


Figure 6

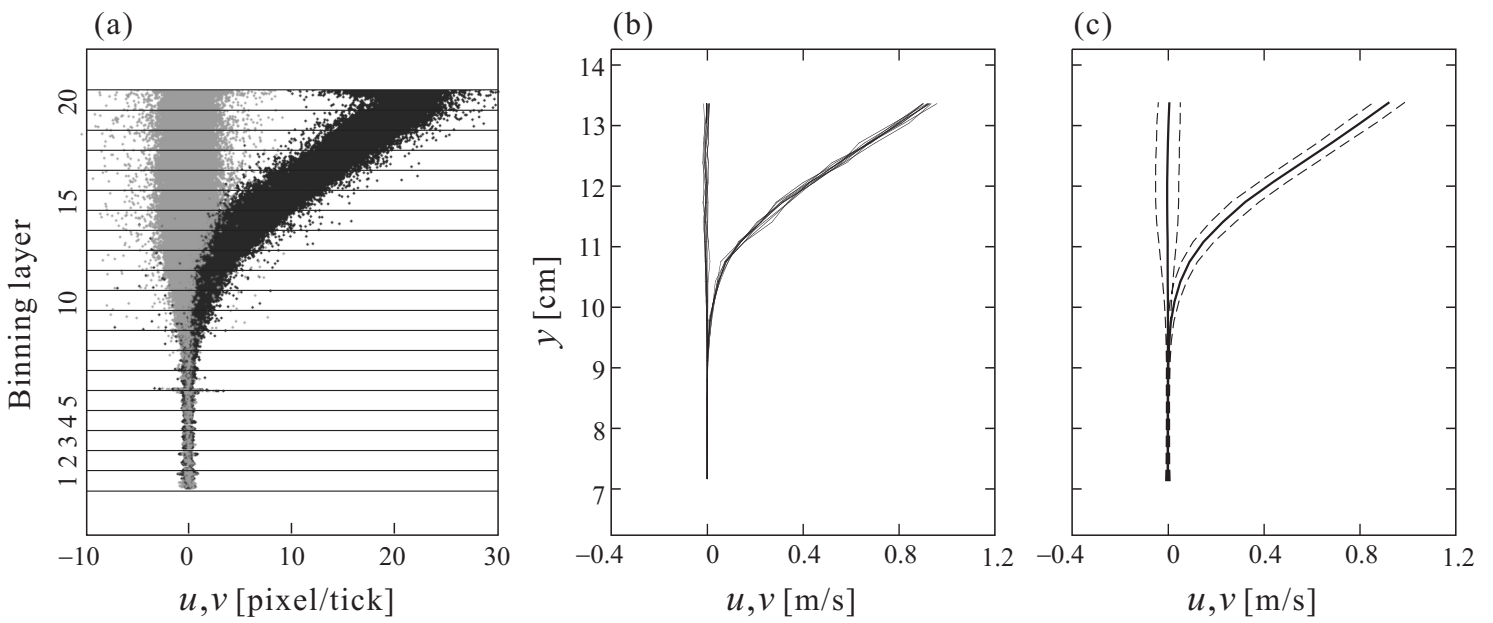


Figure 7

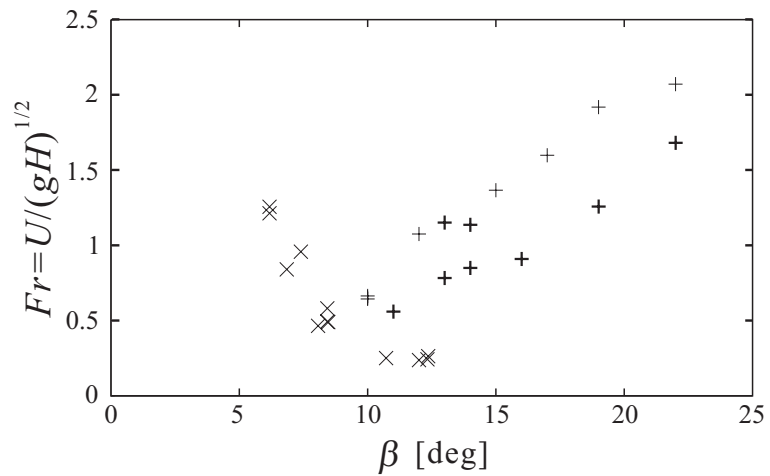


Figure 8

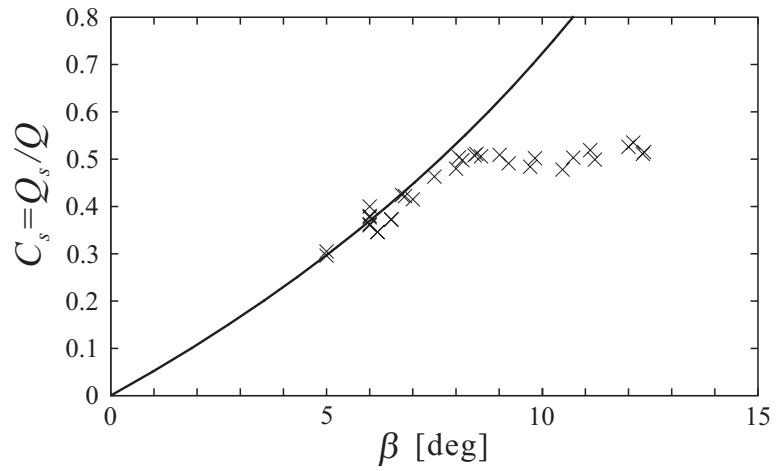


Figure 9

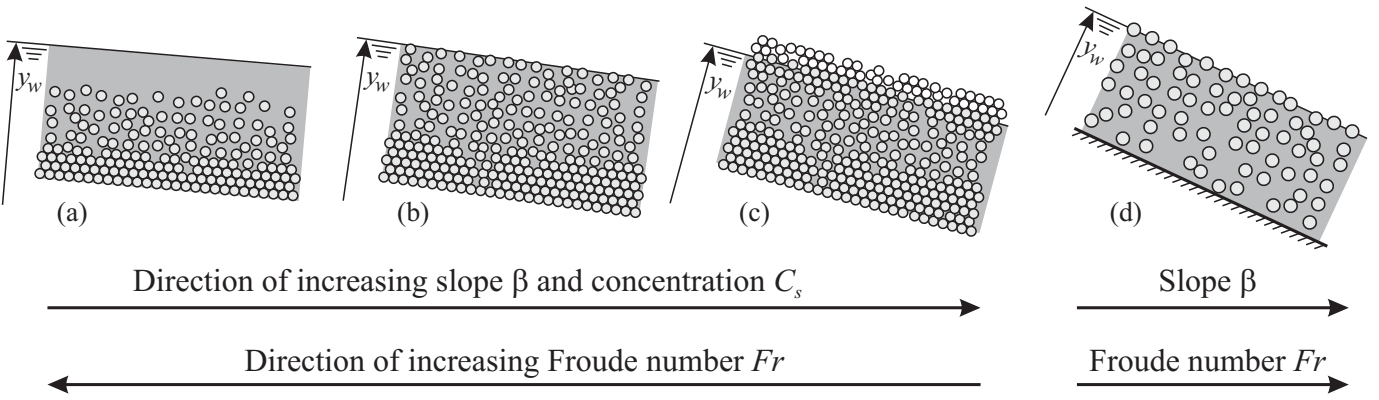


Figure 10

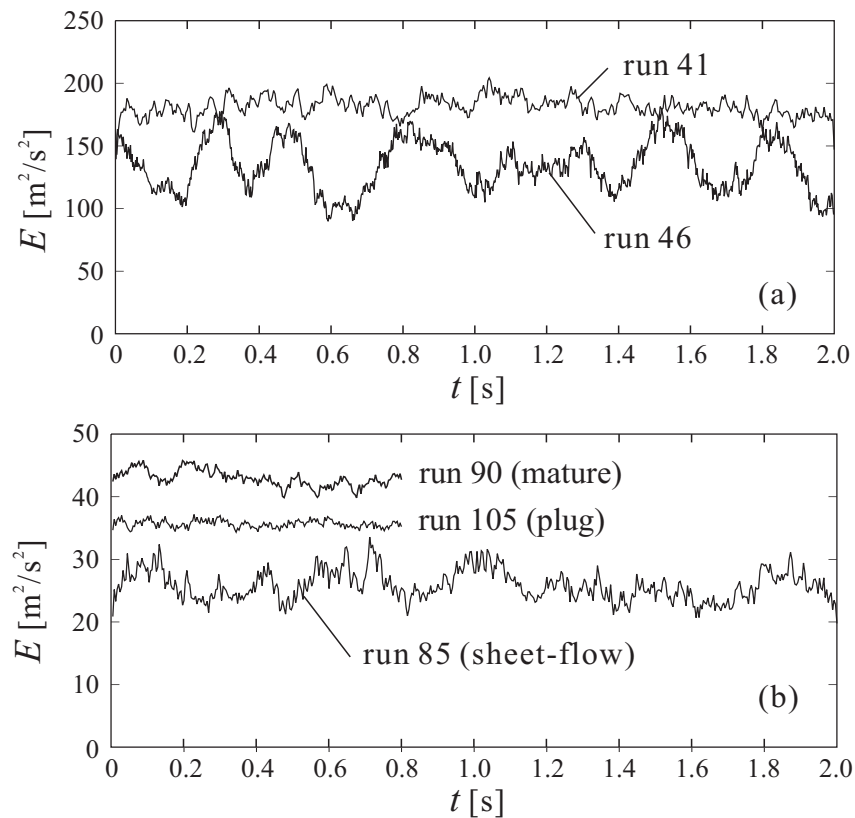


Figure 11

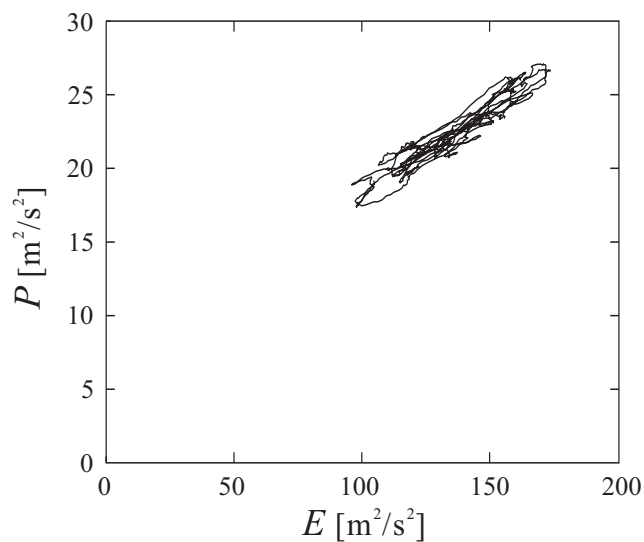


Figure 12

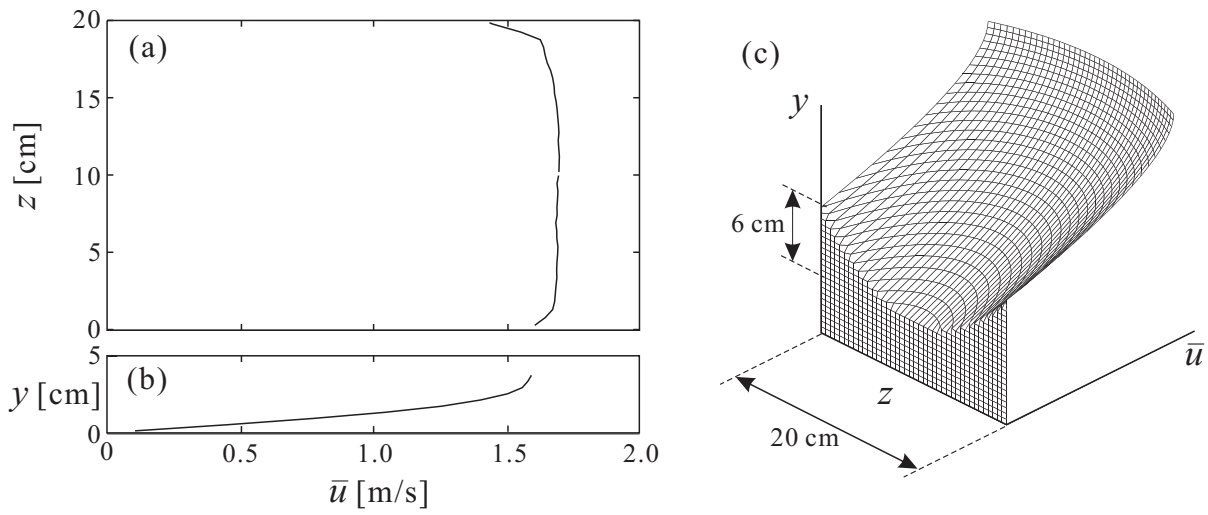


Figure 13

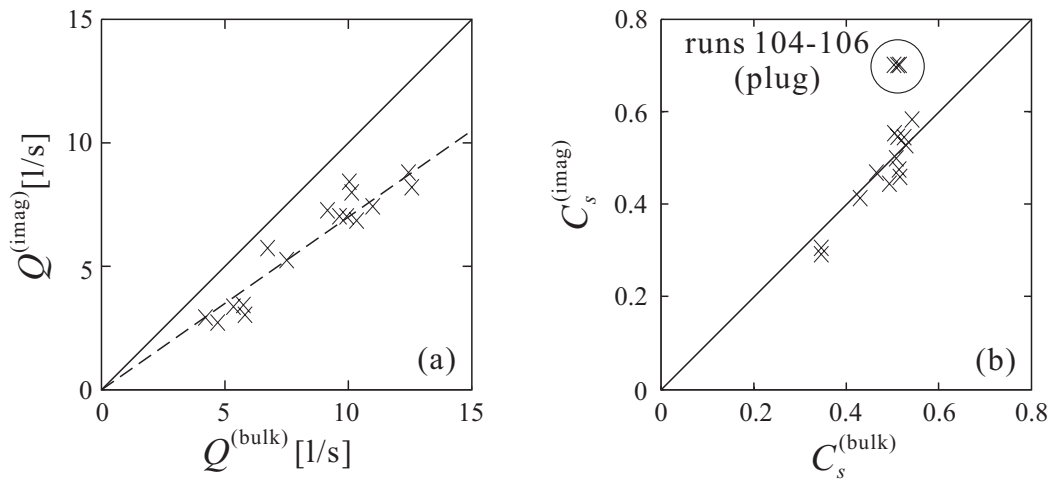


Figure 14

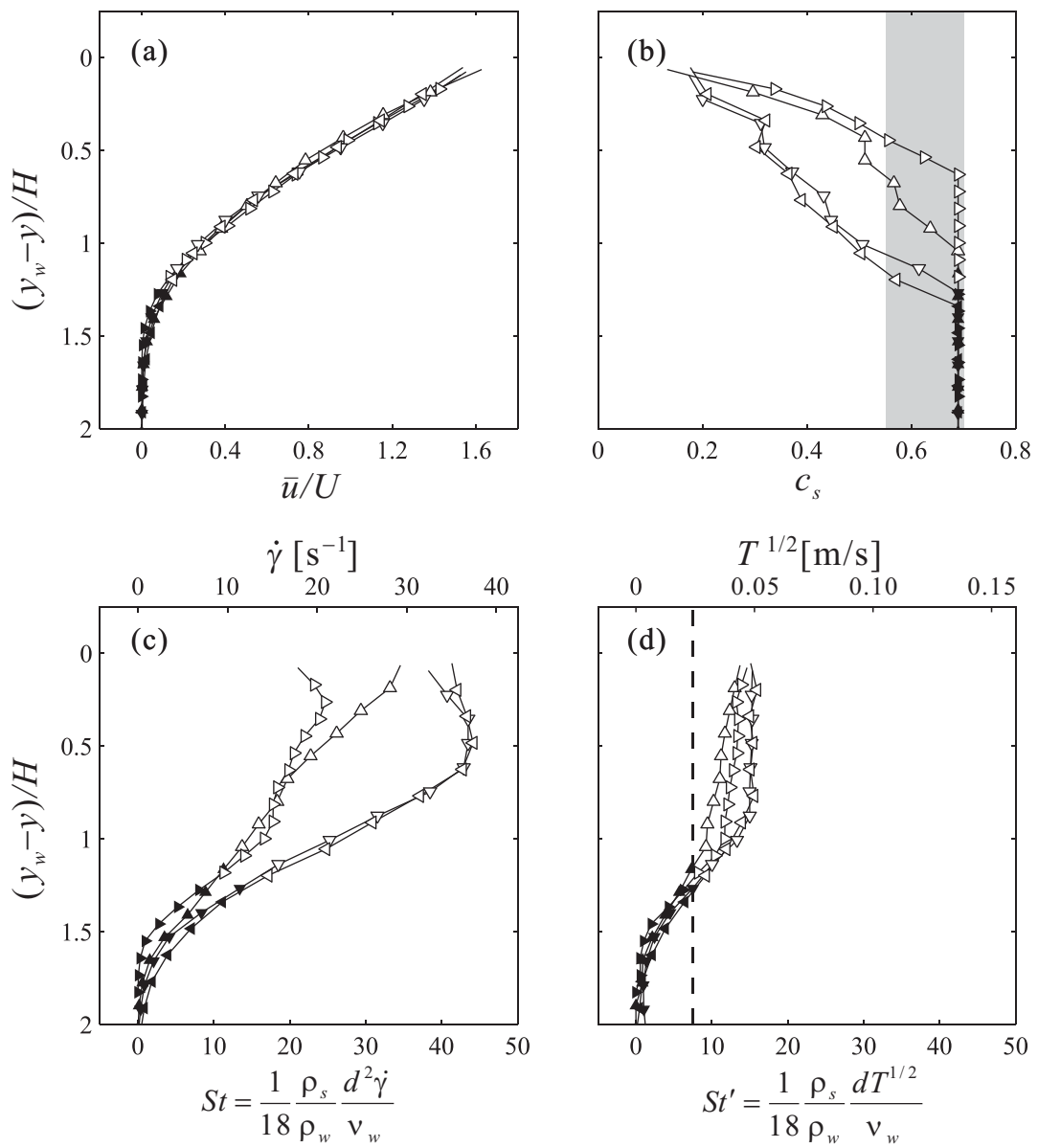


Figure 15

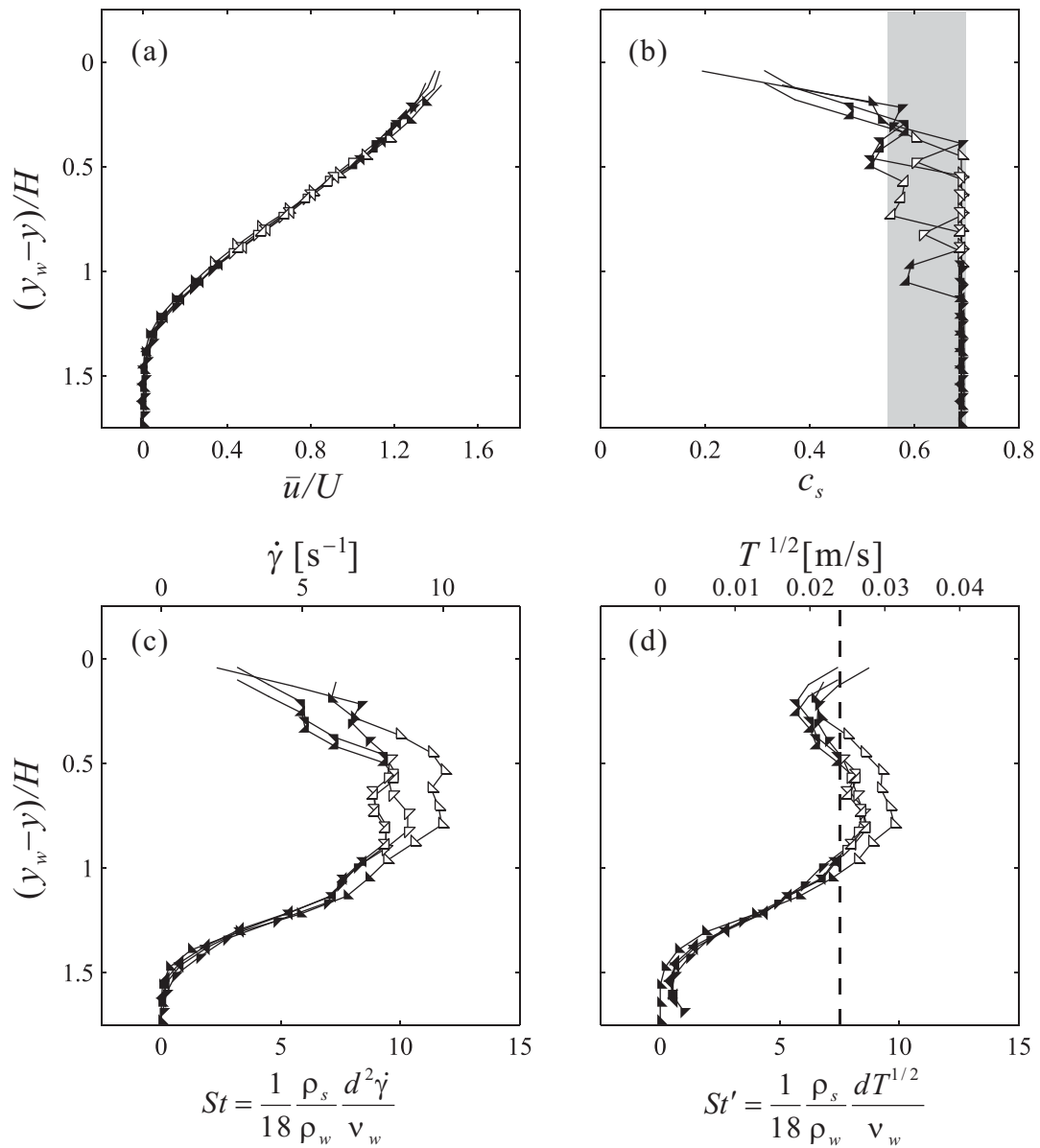


Figure 16

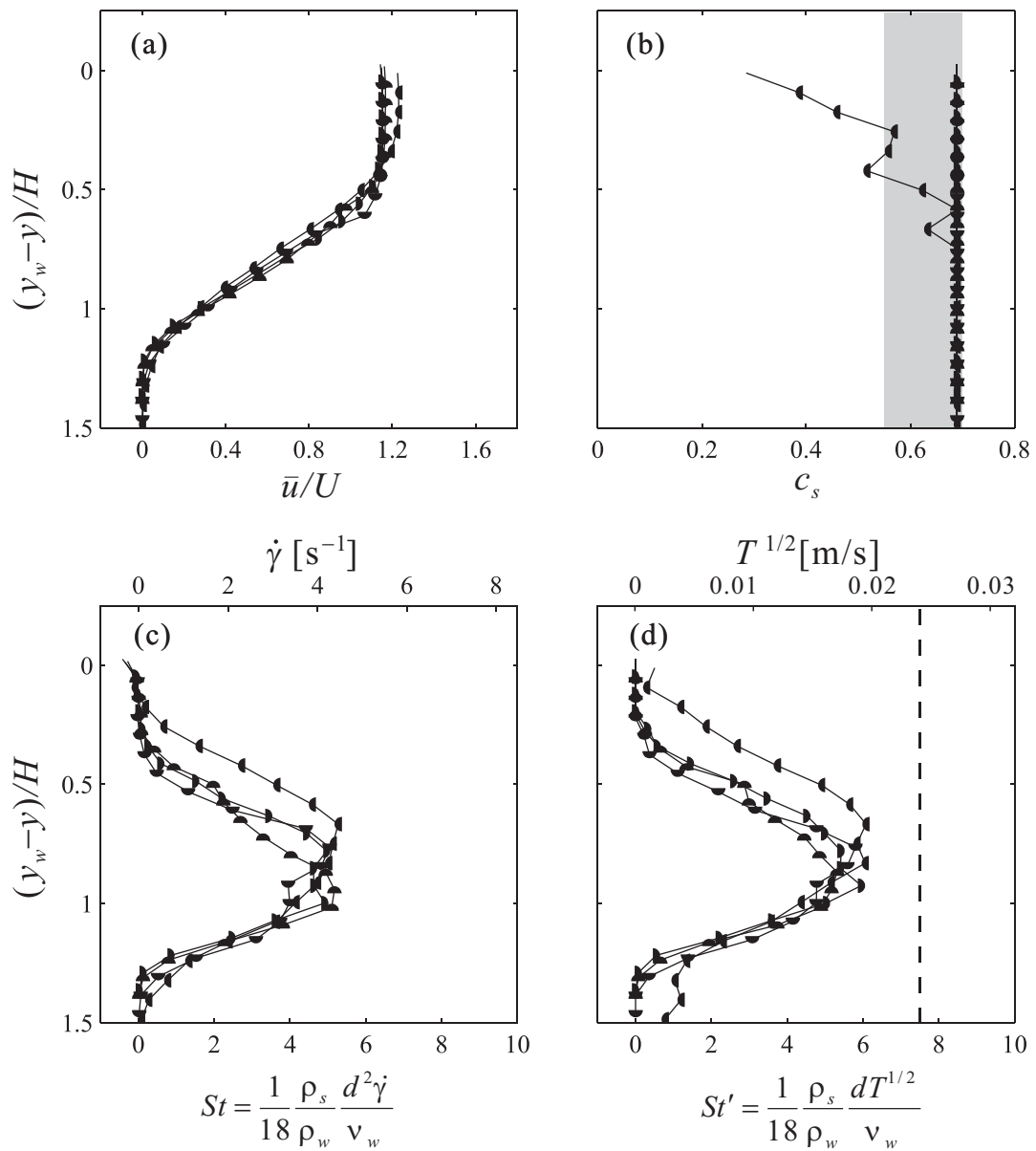


Figure 17

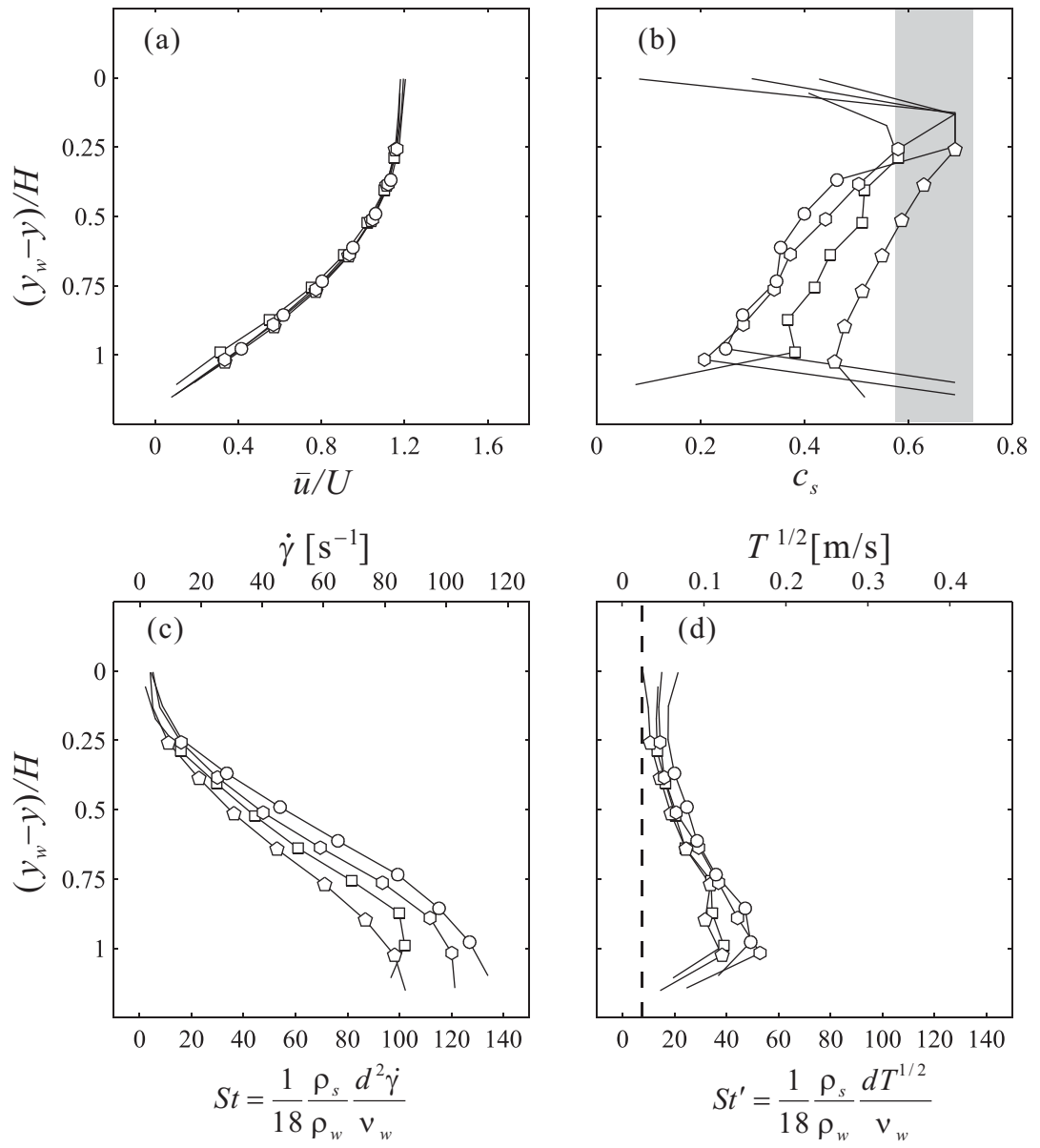


Figure 18

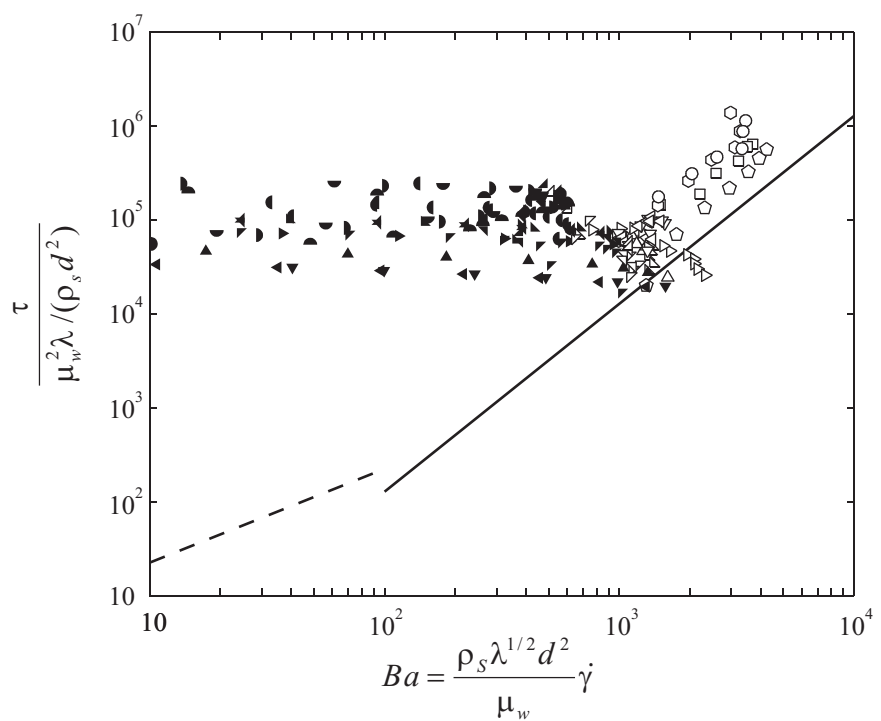


Figure 19

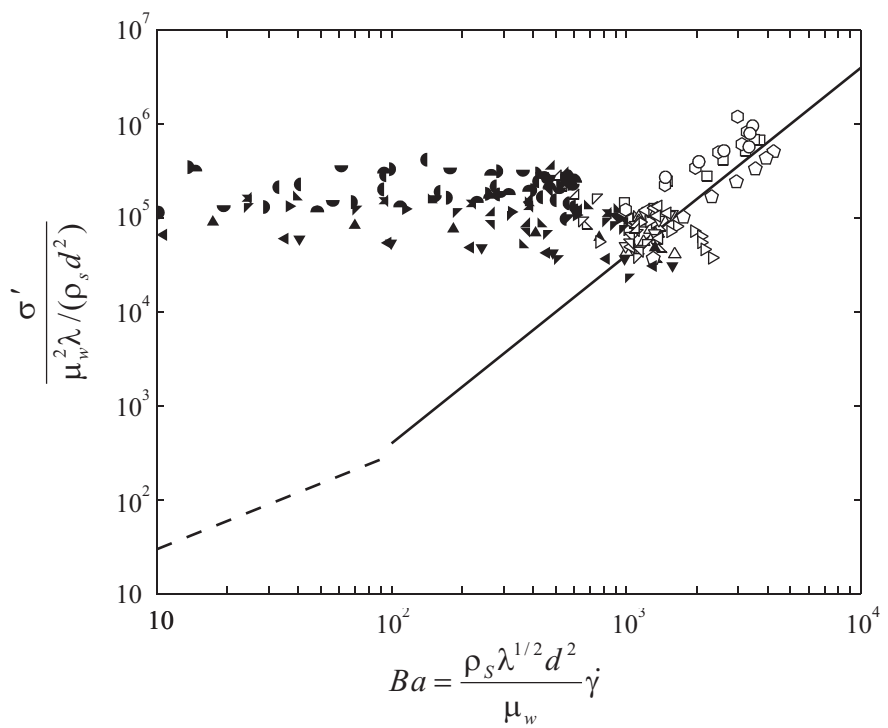


Figure 20

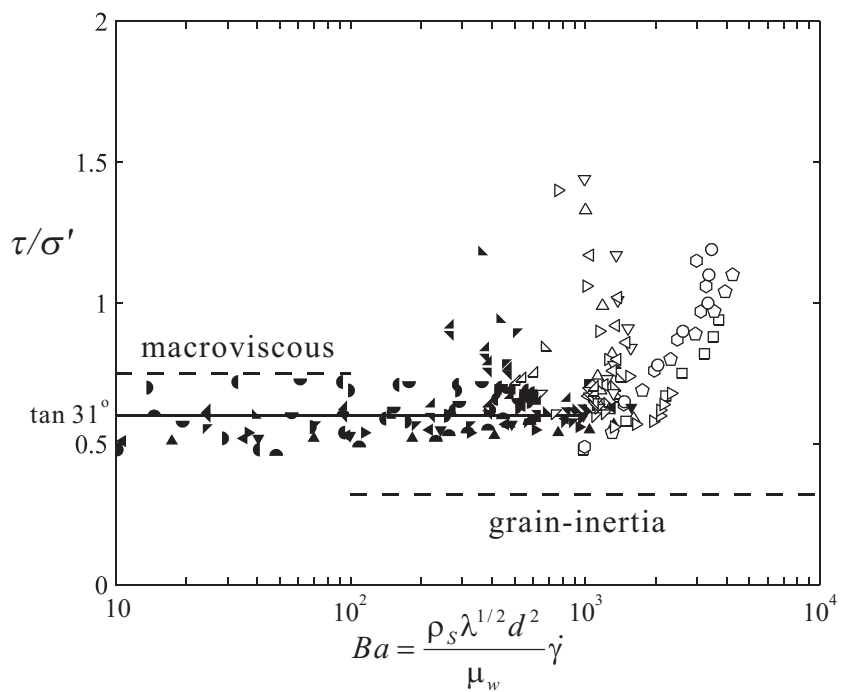


Figure 21

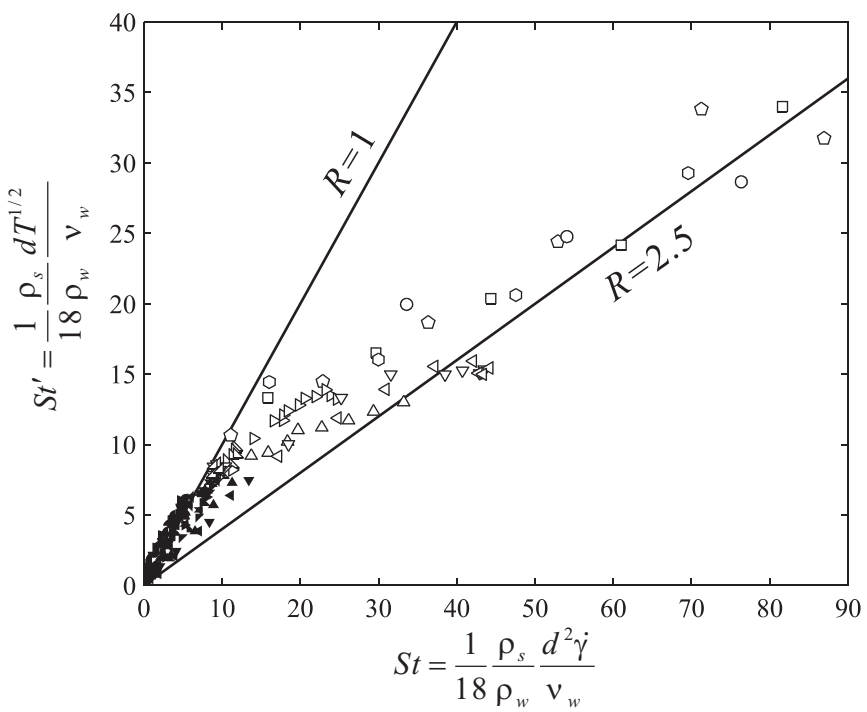


Figure 22

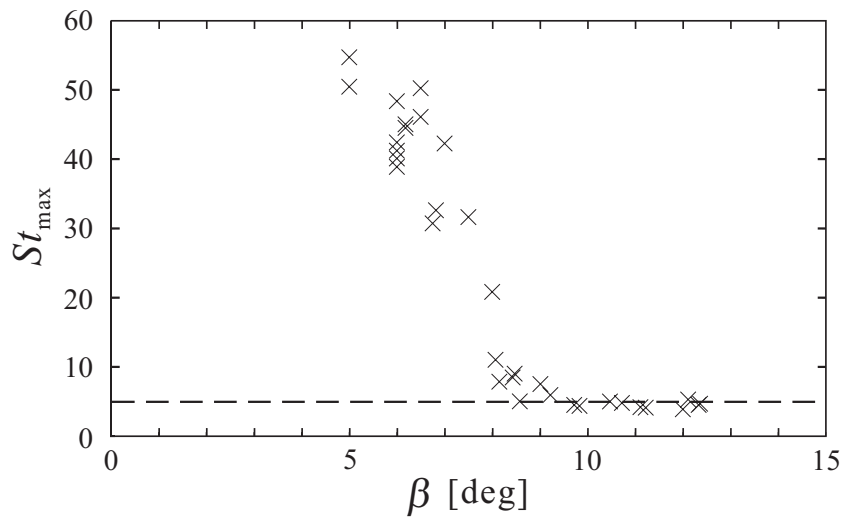


Figure 23

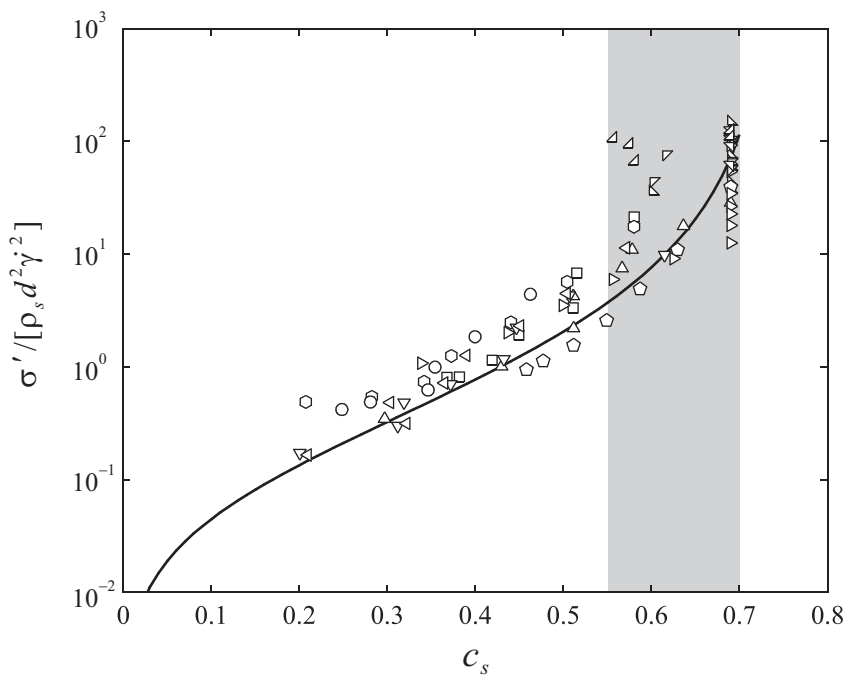


Figure 24

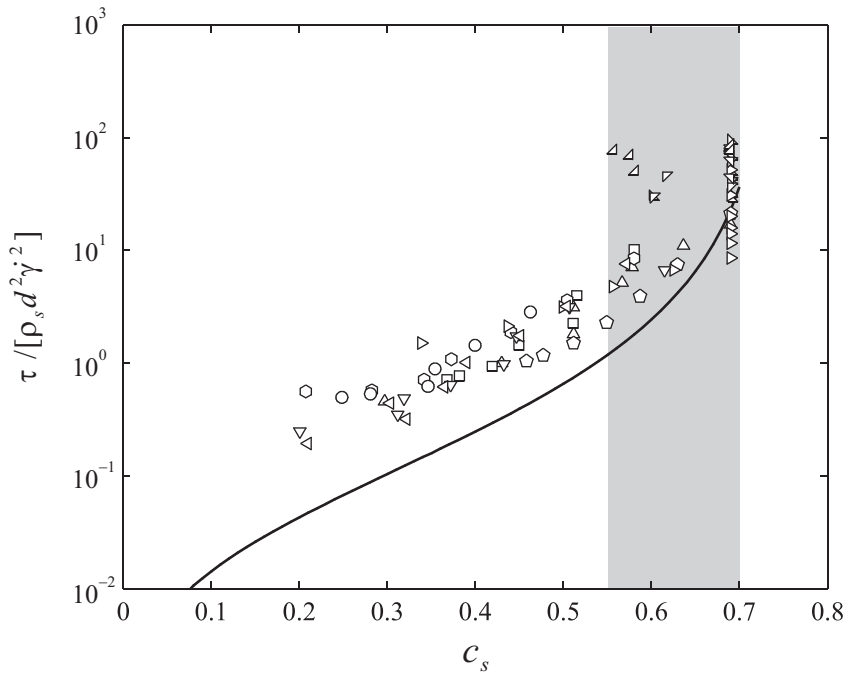


Figure 25

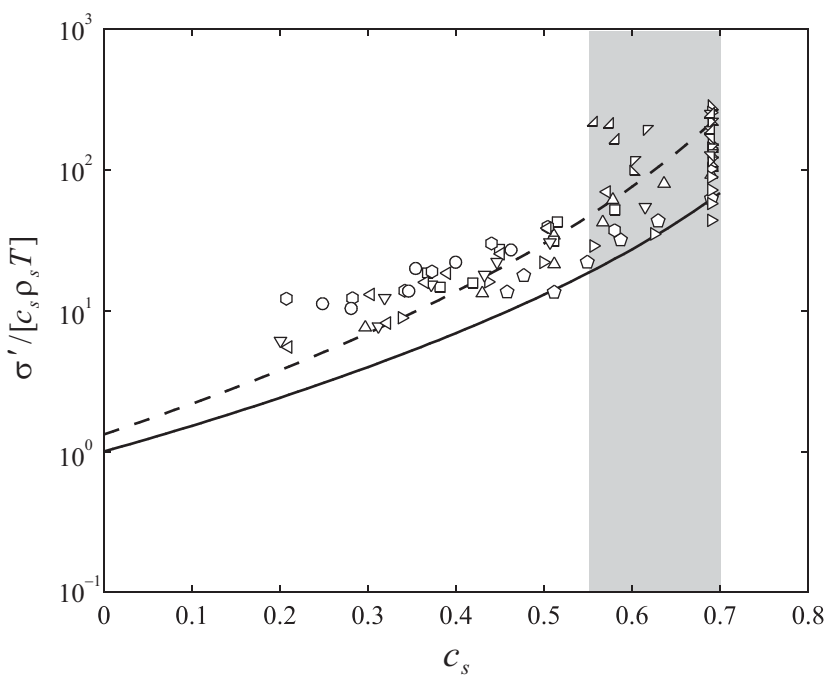


Figure 26

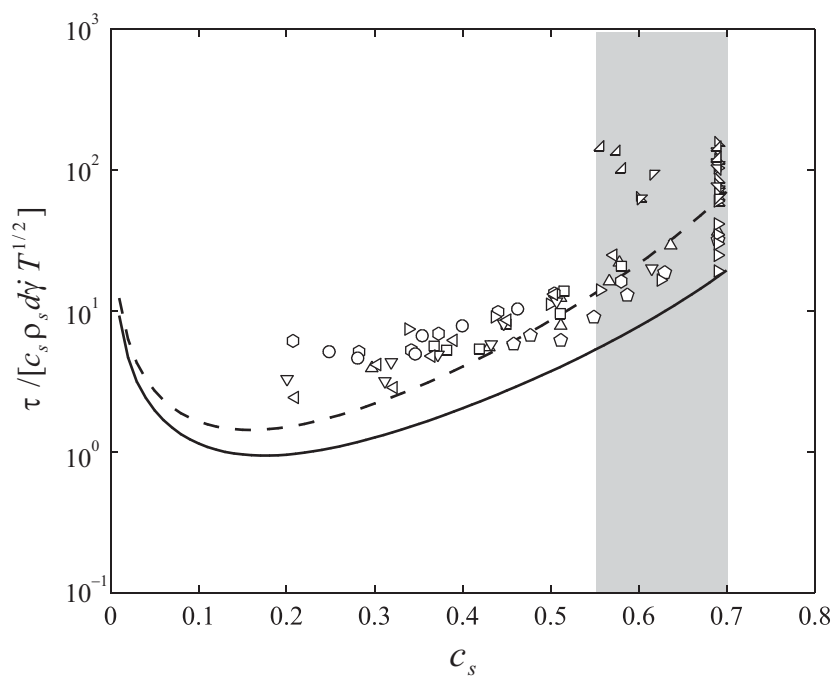


Figure 27

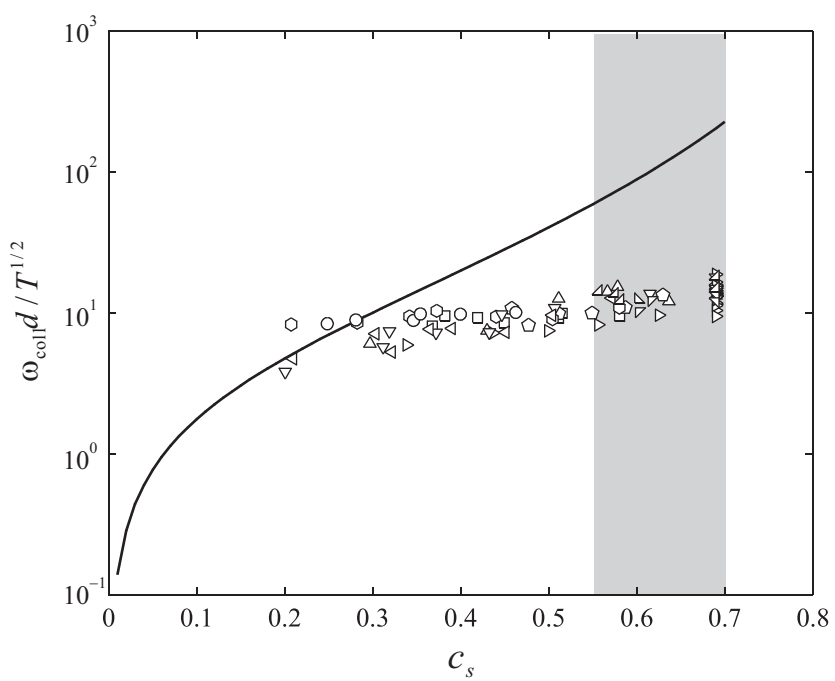


Figure 28

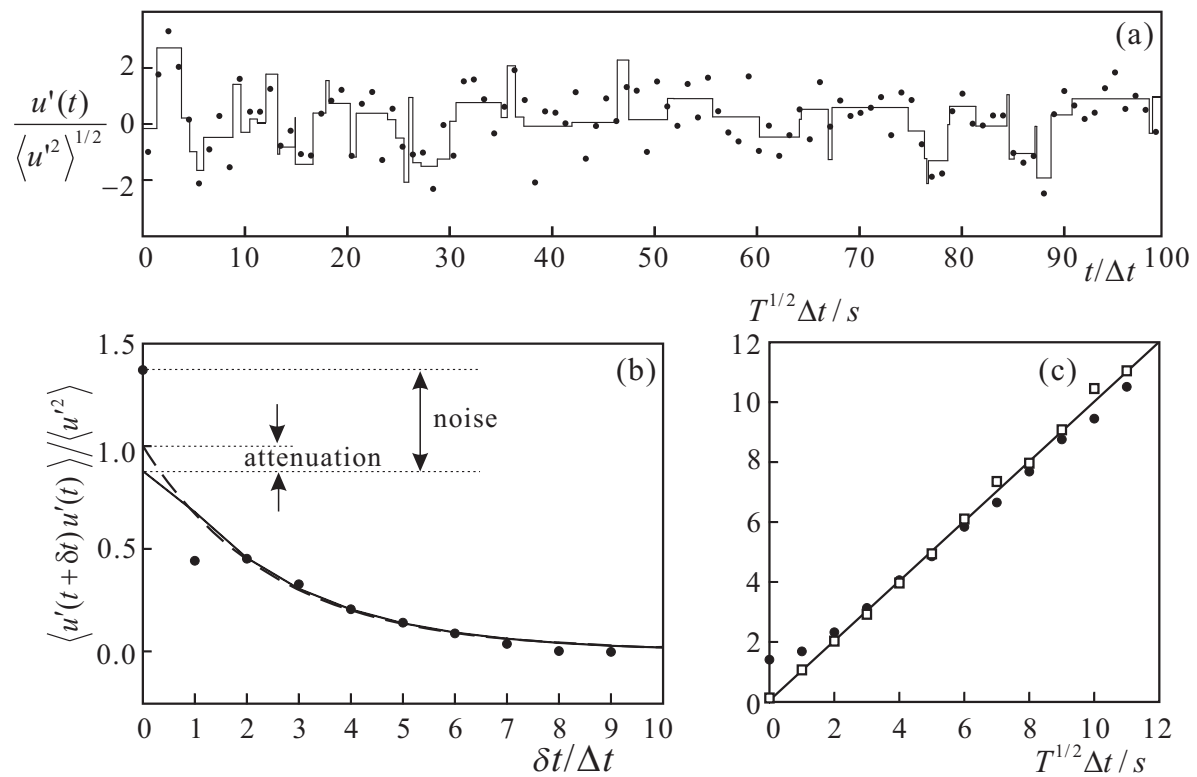


Figure 29

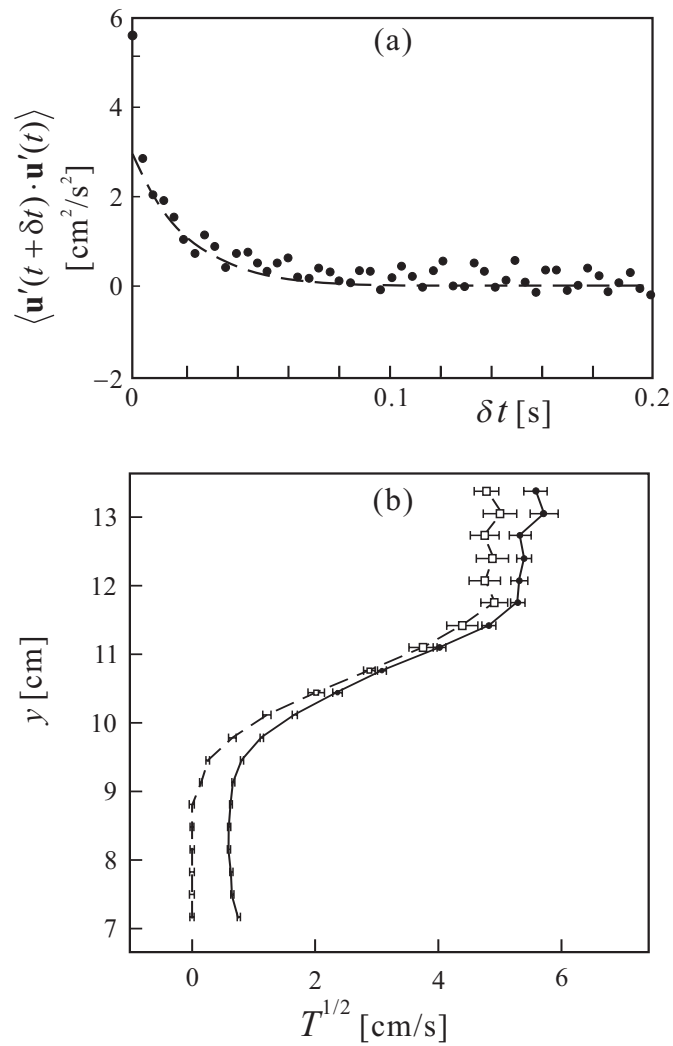


Figure 30